

APPARENT DISK-MASS REDUCTION AND PLANETESIMAL FORMATION IN GRAVITATIONALLY UNSTABLE DISKS IN CLASS 0/I YSOS

Y. TSUKAMOTO^{1,2}, S. OKUZUMI³, AND A. KATAOKA^{4,5}

Draft version March 9, 2022

ABSTRACT

We investigate the dust structure of gravitationally unstable disks undergoing mass accretion from the envelope, envisioning the application to Class 0/I young stellar objects (YSOs). We find that the dust disk quickly settles into a steady state and that, compared to a disk with interstellar medium (ISM) dust-to-gas mass ratio and micron-sized dust, the dust mass in the steady-state decreases by a factor of 1/2 to 1/3, and the dust thermal emission decreases by a factor of 1/3 to 1/5. The latter decrease is caused by dust depletion and opacity decrease owing to dust growth. Our results suggest that the masses of gravitationally unstable disks in the Class 0/I YSOs are underestimated by a factor of 1/3 to 1/5 when calculated from the dust thermal emission assuming an ISM dust-to-gas mass ratio and micron-sized dust opacity, and that a larger fraction of disks in Class 0/I YSOs is gravitationally unstable than was previously believed. We also investigate the orbital radius r_P within which planetesimals form via coagulation of porous dust aggregates and show that r_P becomes ~ 20 AU for a gravitationally unstable disk around a solar mass star. Because r_P increases as the gas surface density increases and a gravitationally unstable disk has a maximum gas surface density, $r_P \sim 20$ AU is the theoretical maximum radius. We suggest that planetesimal formation in the Class 0/I phase is preferable to that in the Class II phase because large gas surface density is expected and large amount of dust is supplied by envelope-to-disk accretion.

1. INTRODUCTION

Class 0/I young stellar objects (YSOs) are in the earliest phase of protostar formation. Recent observations have shown that they possess circumstellar disks (Brinch et al. 2007; Lommen et al. 2008; Takakuwa et al. 2012; Tobin et al. 2012; Murillo et al. 2013; Chou et al. 2014; Ohashi et al. 2014; Sakai et al. 2014; Yen et al. 2014; Aso et al. 2015; Yen et al. 2017). They also possess a gaseous envelope and the envelope-to-disk mass accretion occurs continuously. The lifetimes are estimated to be 0.1 Myr and 0.5 Myr for the Class 0 YSOs and Class I YSOs, respectively (Evans et al. 2009; Williams & Cieza 2011).

Theoretical studies have suggested that gravitationally unstable disks frequently form in Class 0/I YSOs. It is well known that the disk in a Class 0/I YSO easily becomes gravitationally unstable when the magnetic field in the cloud core is sufficiently weak (Nakamoto & Nakagawa 1994; Matsumoto & Hanawa 2003; Vorobyov & Basu 2006; Vorobyov 2009; Vorobyov & Basu 2010b; Machida et al. 2010; Tsukamoto & Machida 2011; Stamatellos et al. 2012; Kimura & Tsuribe 2012; Tsukamoto & Machida 2013; Tsukamoto et al. 2013; Takahashi et al. 2013; Lomax et al. 2014; Tsukamoto et al. 2015c;

Kimura et al. 2016). In particular, Vorobyov and his collaborators investigated disk evolution using long-term simulations (to the end of the Class I phase) and showed that gravitationally unstable disks ubiquitously form in cloud cores in which the magnetic field is negligible. Even when the magnetic field in the cloud core is relatively strong (e.g., when its mass-to-flux ratio normalized by the critical mass-to-flux ratio is an order of unity), a gravitationally unstable disk can form during the Class 0/I YSO phase. Indeed, recent three-dimensional non-ideal magnetohydrodynamics (MHD) simulations suggest that, even with a relatively strong magnetic field, a circumstellar disk forms immediately after protostar formation (Machida et al. 2011; Tsukamoto et al. 2015a,b; Tomida et al. 2015; Masson et al. 2016; Wurster et al. 2016) and becomes gravitationally unstable (Machida et al. 2011; Tsukamoto et al. 2015a,b) (for a review of disk formation in magnetized cloud cores, see Tsukamoto (2016)). In particular, Machida et al. (2011) investigated the long-term evolution of circumstellar disks (until 10^5 years after protostar formation) and showed that gravitationally unstable disks can form even in strongly magnetized cloud cores. Therefore, from a theoretical point of view, gravitationally unstable disks may frequently appear in the Class 0/I phase.

The properties of a gravitationally unstable disk are summarized as follows. Disks exhibit gravitational instability (GI) when their Toomre's Q value (Toomre 1964) fulfills the following condition

$$Q \equiv \frac{c_s \kappa_{\text{ep}}}{\pi G \Sigma_{\text{gas}}} \lesssim 1.4 \quad (1)$$

against non-axisymmetric perturbation (Laughlin & Bodenheimer 1994), where c_s , κ_{ep} , Σ_{gas} , and G are the sound velocity, epicycle frequency, gas

¹ Laboratory of Computational Astrophysics, RIKEN, Saitama, Japan

² Graduate Schools of Science and Engineering, Kagoshima University, Kagoshima, Japan

³ Department of Earth and Planetary Sciences, Tokyo Institute of Technology, Meguro, Tokyo, Japan

⁴ Zentrum für Astronomie der Universität Heidelberg, Institut für Theoretische Astrophysik, Albert-Ueberle-Str. 2, 69120 Heidelberg, Germany

⁵ National Astronomical Observatory of Japan, Mitaka, Tokyo 181-8588, Japan

surface density, and gravitational constant, respectively. To fulfill the Q value criterion, the mass of the disk M_{disk} should be $M_{\text{disk}}/M_{\text{star}} \gtrsim 0.1$, where M_{star} is the mass of the central star. Because GI induces spiral arms and promotes mass and angular momentum transport, it is a candidate mechanism for angular momentum transfer in circumstellar disks (in other words, GI can be source of viscous α (Shakura & Sunyaev 1973)). Some gravitationally unstable disks can fragment, and binaries, brown dwarfs, and wide orbit planets can be formed by such fragmentation (Stamatellos & Whitworth 2008, 2009; Vorobyov & Basu 2010a; Nayakshin 2010; Tsukamoto et al. 2013). Furthermore, the disk fragmentation and subsequent accretion of the fragments onto the central star may explain FU Orionis outbursts (Vorobyov & Basu 2006). Another important property of a gravitationally unstable disk is that its surface density Σ_{gas} is at theoretical upper limit because the GI inevitably develops and reduces Σ_{gas} at $Q \sim 1.4$. It has been shown that the time and azimuthally averaged disk structures are well described by a steady-state viscous disk model with the assumption that $Q = \text{const}$ (e.g., Tsukamoto et al. 2015c). This greatly simplifies the gas disk structure because detailed information about the magnetic field and the ionization degree of the disk are not required.

Although theoretical studies predict that gravitationally unstable disks frequently form in Class 0/I YSOs, observations suggest that most of Class 0/I YSO disks are gravitationally stable. Observations of disk mass estimated from (sub)millimeter dust emissions have shown that disk masses in Class 0/I YSOs are typically $0.01 - 0.1 M_{\odot}$ and the mean disk mass is approximately a few $0.01 M_{\odot}$ (Andrews & Williams 2007; Jørgensen et al. 2009), which is factor of 1/2 to 1/10 smaller than that required to develop GI. Therefore, a discrepancy exists between observation and theoretical prediction.

The source of this discrepancy is unclear. One may imagine that inclusion of magneto-rotational instability (MRI), which is not incorporated (or resolved) in the abovementioned simulations, could remove the discrepancy by promoting further mass accretion. However, we argue that this may not be the case. To clarify this point, we consider the α value at the edge of the disk required to realize a typical mass accretion rate from the envelope of $\dot{M}_{\text{gas}} \sim 10^{-6} M_{\odot} \text{ yr}^{-1}$. Using the viscous accretion disk model (Shakura & Sunyaev 1973), the α value is estimated as

$$\alpha = \frac{\dot{M}_{\text{gas}}}{3\pi\Sigma_{\text{gas}}c_s^2/\Omega} = \frac{1}{3} \frac{\dot{M}_{\text{gas}}}{c_s^3/G} Q = 0.74 \left(\frac{\dot{M}_{\text{gas}}}{10^{-6} M_{\odot} \text{ yr}^{-1}} \right) \left(\frac{Q}{10} \right) \left(\frac{T}{20\text{K}} \right)^{-3/2} \quad (2)$$

where we assume that the typical radius of the disk is $r_{\text{disk}} = 100\text{AU}$ (Williams & Cieza 2011) and that disk temperature is typically 20 K at 100 AU (Chiang & Goldreich 1997). We also assume that $\kappa_{\text{ep}} = \Omega$, where Ω is the angular velocity and $c_s = \sqrt{k_B T/m_g} = 1.9 \times 10^4 (T/10 \text{ K})^{1/2} \text{ cm s}^{-1}$, where k_B and $m_g = 3.9 \times 10^{-24} \text{ g}$ are the Boltzmann constant and mean molecular

mass, respectively. This estimate shows that a quite large α of ~ 1 is required to achieve $\dot{M}_{\text{gas}} = 10^{-6} M_{\odot} \text{ yr}^{-1}$ in a disk with $Q = 10$ and $r_{\text{disk}} = 100 \text{ AU}$. On the other hand, the MRI-induced α is typically $\alpha \sim 10^{-2}$, even in fully ionized disk, and may be significantly smaller when the non-ideal MHD effects are at work (Fleming et al. 2000; Bai & Stone 2011; Kunz & Lesur 2013). Therefore, the angular momentum transfer owing to MRI is too weak to attain the typical mass accretion rate of $\dot{M}_{\text{gas}} = 10^{-6} M_{\odot} \text{ yr}^{-1}$ from the envelope, and the mass inevitably accumulates in the disk. Even for a disk with $Q \sim 2$, which corresponds to a marginally gravitationally unstable disk, α should be ~ 0.14 at 100 AU. Again, MRI may not play a major role in the outer region. Because no physical mechanism is known to produce $\alpha \sim 1$, and because the above estimate is robust and difficult to refute, we conclude that MRI (or other angular momentum transfer mechanisms) may not solve the discrepancy.

Thus, we should seek a source of this discrepancy other than MRI. One possible explanation we pursue in this paper is growth and depletion of the dust particles. Gas disk mass is often estimated from dust thermal emission by assuming the typical dust-to-gas mass ratio of the interstellar medium (ISM), $f_{\text{dg,ISM}} = 1/100$ and micron-sized dust. However, whether these assumptions are also justified for the disk is unclear because dust particles can grow and can be depleted by radial migration. The reduction of the dust-to-gas mass ratio causes an apparent underestimation of the gas mass. Furthermore, dust opacity can decrease by dust growth, which also leads to an apparent underestimation of the gas mass. The problem of assuming the ISM dust-to-gas mass ratio and simply converting the dust mass to a gas mass have been pointed out by several authors (Kamp et al. 2005; Dullemond & Dominik 2005; Brauer et al. 2007; Dunham et al. 2014). In fact, the disk observations using HD line emission, which is a more direct tracer for disk mass suggest that the disk mass estimated from dust thermal emission tends to be smaller (Bergin et al. 2013; McClure et al. 2016). Note also that Andrews & Williams (2007) (see also Hartmann et al. 1998) pointed out that the disk mass required to maintain disk-to-star mass accretion during the Class II phase is much larger than that estimated from dust thermal emission. Although these previous studies mostly focus on the Class II phase, dust growth and depletion also possibly explain the discrepancy of disk mass in Class 0/I YSOs.

Several observational studies have suggested the dust growth occurs in YSOs. (Beckwith & Sargent 1991; Kitamura et al. 2002; Jørgensen et al. 2007; Kwon et al. 2009; Ricci et al. 2010a,b; Pérez et al. 2012; Miotello et al. 2014; Tobin et al. 2013; Pérez et al. 2015; Tazzari et al. 2016; Carrasco-González et al. 2016). It is known that the opacity spectral index β decreases owing to dust growth. For example, Ricci et al. (2010a) showed that the Class II YSOs in Ophiuchus exhibit $\beta \sim 0.5$, which is significantly smaller than the ISM value, i.e., $\beta 1.7$. Even in Class 0/I YSOs, the value of β can be smaller than that in the ISM (Jørgensen et al. 2007; Kwon et al. 2009; Tobin et al. 2013). These observations suggest that dust growth occurs ubiquitously in disks (here, we assume that a dust disk is optically thin

for millimeter wavelengths) and that the dust size may be significantly larger than that in the ISM. In particular, small β observed in some Class 0 YSOs suggests that the dust growth occurs even in the earliest phase of star formation. Note, however, that we should take care in interpreting these observations because β also decreases when the disk is optically thick. As shown by the recent observation of a Class I object (Cieza et al. 2016), it is possible that the decreases in the value of β comes not from dust growth but from the large optical depth of the disk. Thus, verifications of dust growth in Class 0/I objects by future high-resolution observations are awaited.

From a theoretical point of view, dust growth and subsequent dust radial drift are also expected even in the Class 0/I phase because of the small timescale of dust growth and radial drift. Previous studies have pointed out that the growth and drift timescales of dust particles are much smaller than the viscous timescale of the disk (Weidenschilling 1977; Nakagawa et al. 1986; Takeuchi et al. 2005) and the dust-to-gas mass ratio decreases in a very short duration (Dullemond & Dominik 2005; Brauer et al. 2007, 2008). In these previous studies, however, isolated disks were investigated and how dust evolution proceeds in Class 0/I phase (or under the envelope-to-disk accretion) was not clear. More recently, Birnstiel et al. (2010) investigated the evolution of dust particles in an evolving circumstellar disk by considering the envelope-to-disk mass accretion. They showed that the dust-to-gas mass ratio become as small as $\sim 1/1000$ at $t = 1$ Myr after the simulation was initiated, with the collisional fragmentation being negligible. Although Birnstiel et al. (2010) clearly showed the possibility of significant reduction of the dust-to-gas mass ratio at the end of the Class I phase, the quantitative reduction rate of the dust-to-gas mass ratio during the Class 0/I phase was not shown. Furthermore, the dependence of the reduction rate on parameters, such as mass accretion rate onto the disk, mass of the central star, dust porosity, and the gas disk structure, remains unclear.

Another important issue regarding dust evolution in a gravitationally unstable disk is the maximum orbital radius of planetesimal formation. Okuzumi et al. (2012) and Kataoka et al. (2013) proposed a planetesimal formation scenario in which icy planetesimals form from highly porous dust aggregates. In their scenario, as noted by Okuzumi et al. (2012), the orbital radius within which planetesimals form is an increasing function of the gas surface density. On the other hand, the gas surface density of a gravitationally unstable disk is the theoretical upper limit. Therefore, we can determine the maximum orbital radius within which planetesimals form by considering planetesimal formation in a gravitationally unstable disk.

In this paper, we investigate the dust structure and planetesimal formation in gravitationally unstable disks undergoing mass accretion from envelopes. This paper is organized as follows: In §2, we describe the models and governing equations for dust evolution. The results are given in §3. We summarize and discuss our results in §4.

2. MODELS

In this section, we describe the gas disk model and the governing equations for dust evolution adopted in this paper. To clarify the dust evolution in a gas disk

and simplify the system behavior, we assume that the gas disk is in a steady state and does not evolve. As discussed in this section, this assumption is valid.

2.1. Steady-state structure of gravitationally unstable disks

We construct the steady-state profile of a gravitationally unstable disk as a function of the radius r , mass of the central star M_{star} , and mass accretion rate of gas \dot{M}_{gas} . The fundamental assumptions of our disk model are as follows:

1. The disk can be described by the viscous α accretion disk model (Shakura & Sunyaev 1973);
2. The disk is steady, meaning that $\dot{M}_{\text{gas}} = \text{const}$;
3. The Toomre's Q value of the disk is on the order of unity and constant.

With these assumptions, the physical quantities of the disk should satisfy the following equation:

$$\left| \frac{d \ln \Omega}{d \ln R} \right| \alpha \frac{c_s^2}{\Omega} \Sigma_{\text{gas}} = \frac{1}{2\pi} \dot{M}_{\text{gas}} = \text{const.} (\propto r^0), \quad (3)$$

where, \dot{M}_{gas} is the mass accretion rate of the gas, $\alpha = \nu \frac{\Omega}{c_s^2}$, and ν is the kinematic viscosity. The Q value for a marginally gravitationally unstable disk takes constant value Q_{crit} ,

$$Q = Q_{\text{crit}} (\propto r^0). \quad (4)$$

We set $Q_{\text{crit}} = 2$ because spiral arms develop at $Q \sim 1.4$ (Laughlin & Bodenheimer 1994) and a marginally unstable disk may have a slightly larger Q value than 1.4. Here and in the following, we approximate the epicycle frequency as $\kappa_{\text{ep}} = \Omega$.

Equations (3) and (4) yield

$$\begin{aligned} \Sigma_{\text{gas}} &\propto T^{1/2} \Omega, \\ \alpha &\propto \dot{M}_{\text{gas}} T^{-3/2}, \end{aligned} \quad (5)$$

where we have used $c_s \propto T^{1/2}$. Thus, from equations (3) and (4), we can determine the profile of the gravitationally unstable steady disk by specifying a rotation profile, temperature profile (or energy balance equation), and mass accretion rate.

In this paper, we assume the Keplerian rotation as

$$\Omega = \sqrt{\frac{GM_{\text{star}}}{r^3}}, \quad (6)$$

for simplicity. Note, however, that the rotational profile of a gravitationally unstable disk may differ from simple Keplerian rotation, because the gravitational potential is modified from that of the point gravity source by the disk self-gravity (see, Tsukamoto et al. 2015c).

2.1.1. Temperature profile

We assume that the disk temperature T is determined by the stellar irradiation and obeys the profile given in Kusaka et al. (1970) and Chiang & Goldreich (1997) as

$$T = T_{\text{irr}} \equiv 150 \left(\frac{r}{1 \text{ AU}} \right)^{-3/7}. \quad (7)$$

The assumption that the disk temperature is determined by irradiation is valid because the viscous heating is negligible for $r \gtrsim 10$ AU which is our primary focus. In Appendix B, we estimate the temperature profile determined by the viscous heating and confirm that the viscous heating is negligible.

2.1.2. Gas disk structure

By solving equations (3), (4), (6), and (7), we obtain the steady-state solution for the gravitationally unstable gas disk as

$$\Sigma_{\text{gas}} = 1.3 \times 10^1 \left(\frac{M}{M_{\odot}} \right)^{1/2} \left(\frac{r}{100 \text{ AU}} \right)^{-12/7} \text{ g cm}^{-2}, \quad (8)$$

$$\alpha = 1.4 \times 10^{-1} \left(\frac{\dot{M}_{\text{gas}}}{10^{-6} M_{\odot} \text{ yr}^{-1}} \right) \left(\frac{r}{100 \text{ AU}} \right)^{9/14}. \quad (9)$$

Note that α has a radial dependence of $\alpha \propto r^{9/14}$, which is a general feature of realistic disks.

The diffusion timescale of our disk is estimated as

$$t_{\text{diff}} \equiv \frac{r^2}{\nu} = 1.4 \times 10^5 \left(\frac{r}{100 \text{ AU}} \right)^{2/7} \left(\frac{\dot{M}_{\text{gas}}}{10^{-6} M_{\odot} \text{ yr}^{-1}} \right)^{-1} \left(\frac{M_{\text{star}}}{M_{\odot}} \right)^{1/2} \text{ years} \quad (10)$$

where $\nu = \alpha c_s^2 / \Omega$ is the kinematic viscosity. This value is smaller than or comparable to the lifetime of the Class 0/I phase ~ 0.5 Myr, and our assumption of the steady-state is valid.

2.1.3. Assumptions for the viscous α

We assume that α values that lead to the gas advection and internal turbulence are identical for simplicity. While the former includes both turbulent viscosity and gravitational torque, i.e., $\alpha_{\text{turb}} + \alpha_{\text{grav}}$. The latter incorporates α_{turb} only. Here $\alpha_{\text{turb}} = \langle \Sigma_{\text{gas}} \delta v_R \delta v_{\phi} \rangle$ is the α value induced by the Reynolds stress. and $\alpha_{\text{grav}} = \langle \int dz g_R g_{\phi} / (4\pi G) \rangle$ is that induced by the gravitational torque, where $\langle \rangle$ indicates the time and azimuthal average, and δv_R , δv_{ϕ} and g_R , g_{ϕ} indicate the radial and azimuthal components of the velocity fluctuation and of the gravitational force induced by the spiral arms, respectively. This simplification is valid if $\alpha_{\text{turb}} / \alpha_{\text{grav}} \gg 1$. Note that, with this simplification, we overestimate the collision velocity induced by the disk turbulence, and the realistic collision velocity is smaller than the value obtained in this paper. We neglect the effect of MRI, because it is expected to be weak ($\alpha \lesssim 10^{-2}$) compared to the GI in the outer region ($\alpha \sim 10^{-1}$).

2.2. Dust model

An important quantity that determines the dust dynamics is the stopping time of dust particles t_s , which is the timescale on which the dust particle momentum is relaxed by gas drag. In this paper, we consider two regimes of the stopping time depending on the dust size:

$$t_s = \begin{cases} \frac{\rho_{\text{int}} a_{\text{dust}}}{\rho_{\text{gas}} v_{\text{th}}} & a_{\text{dust}} < \frac{9}{4} \lambda_{\text{mfp}} \quad (\text{Epstein drag law}) \\ \frac{4\rho_{\text{int}} a_{\text{dust}}}{9\rho_{\text{gas}} v_{\text{th}} \lambda_{\text{mfp}}} & a_{\text{dust}} > \frac{9}{4} \lambda_{\text{mfp}} \quad (\text{Stokes drag law}) \end{cases} \quad (11)$$

where ρ_{int} , a_{dust} , and ρ_{gas} are the internal density, radius of the dust particles, and gas density, respectively. We adopt $\rho_{\text{int}} = 1.4f \text{ g cm}^{-3}$ where f is volume filling factor. The thermal velocity v_{th} is given by $v_{\text{th}} = \sqrt{8/\pi} c_s$. The mean free path is given by $\lambda_{\text{mfp}} = m_{\text{gas}} / (\sigma_{\text{mol}} \rho_{\text{gas}})$, where $\sigma_{\text{mol}} = 2 \times 10^{-15} \text{ cm}^2$ is the collisional cross section of the gas molecules and $m_{\text{gas}} = 3.9 \times 10^{-24} \text{ g}$ is the mean molecular mass. We do not consider Newton's drag regime, which applies to very large particles around which the gas flow has high Reynolds numbers. The motion of the dust particles is characterized by the Stokes number St , which is defined as

$$\text{St} \equiv \Omega t_s = \begin{cases} \frac{\pi \rho_{\text{int}} a_{\text{dust}}}{2 \Sigma_{\text{gas}}}, & a_{\text{dust}} < \frac{9}{4} \lambda_{\text{mfp}} \quad (\text{Epstein drag law}), \\ \frac{2 \rho_{\text{int}} a_{\text{dust}}^2}{9 \Sigma_{\text{gas}} \lambda_{\text{mfp}}}, & a_{\text{dust}} > \frac{9}{4} \lambda_{\text{mfp}} \quad (\text{Stokes drag law}). \end{cases} \quad (12)$$

In this study, we employ simplified dust coagulation equations in which the dust size distribution is characterized by the single representative mass $m_{\text{dust}}(r)$. This single-size approximation have been employed in many previous studies on dust evolution in protoplanetary disks (Kornet et al. 2001; Birnstiel et al. 2012; Sato et al. 2016; Okuzumi et al. 2016; Krijt et al. 2016). The governing equations for dust evolution are

$$\frac{\partial \Sigma_{\text{dust}}}{\partial t} + \frac{1}{r} \frac{\partial}{\partial r} (r v_{r,\text{dust}} \Sigma_{\text{dust}}) = 0, \quad (13)$$

$$\frac{\partial m_{\text{dust}}}{\partial t} + v_{r,\text{dust}} \frac{\partial m_{\text{dust}}}{\partial r} = \frac{m_{\text{dust}}}{t_{\text{coll}}}, \quad (14)$$

where Σ_{dust} and $v_{r,\text{dust}}$ are the dust surface density and the dust radial velocity, respectively. The first equation represents the mass conservation of dust particles, where we neglect the turbulent diffusion term for simplicity. In this paper, we consider two forms for the dust radial velocity. One is the standard form, which is given as

$$v_{r,\text{dust}} = - \left(\frac{v_{r,\text{gas}}}{1 + \text{St}^2} + \frac{2\text{St}}{1 + \text{St}^2} \eta v_K \right), \quad (15)$$

where $v_K = r\Omega$, $v_{r,\text{gas}}$ is the gas radial velocity given as $v_{r,\text{gas}} = \dot{M}_{\text{gas}} / (2\pi r \Sigma_{\text{gas}})$, and η is a parameter that determines the sub-Kepler motion of the gas and is expressed as (Weidenschilling 1977),

$$\eta = -\frac{1}{2} \left(\frac{c_s}{v_K} \right)^2 \frac{d \ln P}{d \ln r}. \quad (16)$$

The first and second terms in the right hand side describe the dust radial motion caused by gas advection (Kornet et al. 2001) and the radial drift of the dust particles (Weidenschilling 1977), respectively. We also consider the other form for the dust radial velocity, which is given by

$$v_{r,\text{dust}} = - \left(v_{r,\text{gas}} + \frac{2\text{St}}{1 + \text{St}^2} \eta v_K \right). \quad (17)$$

In this form, the radial drift caused by gas advection is artificially enhanced for $\text{St} \gtrsim 1$. The reason why we consider this form is to investigate the orbital radius of planetesimal formation in the steady-state solution. When $v_{r,\text{dust}}$ is calculated using equation (15), the radial migration of planetesimals essentially stops because their

Stokes number is $St \gg 1$, and the orbital radius within which planetesimals form r_P is inevitably influenced by the initial condition. The radius of the planetesimal formation calculated using equation (15) indicates the maximum radius of planetesimal formation $r_{P,\max}$ during the time evolution of the dust disk for a given parameter set because the initial disk has a larger dust surface density and larger dust mass accretion rate than are presented in the steady disk. On the other hand, when $v_{r,\text{dust}}$ is calculated using equation (17), the planetesimals migrate with gas advection velocity and are swept away from the disk. Therefore, r_P obtained with equation (17) is the planetesimal formation radius expected from the steady-state solution. We denote this radius as $r_{P,\text{steady}}$, which corresponds to the minimum value of r_P for a given parameter set.

In a realistic situation, whether the planetesimals form at $r_{P,\max}$ or $r_{P,\text{steady}}$ is unclear, in fact, it largely depends on the formation process of the gas disk. If the disk formation process is sufficiently rapid and the disk maintains the ISM dust-to-gas mass ratio, the planetesimals form at $r_{P,\max}$. On the other hand, they form at $r_{P,\text{steady}}$ if the disk formation process is slow and the dust particles are already depleted in the inner region. We can expect, however, that planetesimals form between $r_{P,\max}$ and $r_{P,\text{steady}}$.

Note that the results other than r_P discussed in this paper are independent of the choice of the dust radial velocity. We therefore use equation (15) unless otherwise noted.

Equation (14) represents the dust growth that can be derived by taking the first moment of the dust coagulation equation (see the Appendix of Sato et al. 2016). The collision time t_{coll} is given as

$$t_{\text{coll}} = \frac{1}{4\pi a_{\text{dust}}^2 n_{\text{dust}} \Delta v}. \quad (18)$$

where n_{dust} is the dust number density and Δv is the collision velocity between dust particles. n_{dust} can be rewritten using Σ_{dust} , the dust scale height H_{dust} , and the mass of the dust aggregate m_{dust} as

$$n_{\text{dust}} = \frac{\Sigma_{\text{dust}}}{\sqrt{2\pi} H_{\text{dust}} m_{\text{dust}}}. \quad (19)$$

By assuming a balance between vertical settling and turbulent diffusion, the dust scale height is given as (Dubrulle et al. 1995; Youdin & Lithwick 2007),

$$H_{\text{dust}} = \left(1 + \frac{St}{\alpha} \frac{1 + 2St}{1 + St}\right)^{-1/2} H_{\text{gas}}, \quad (20)$$

where $H_{\text{gas}} = c_s/\Omega$ is the gas scale height. We assume that the collision velocity of the dust particles is given as

$$\Delta v = \sqrt{\Delta v_B^2 + \Delta v_r^2 + \Delta v_\phi^2 + \Delta v_z^2 + \Delta v_{\text{turb}}^2}, \quad (21)$$

where Δv_B , Δv_r , Δv_ϕ , Δv_z and Δv_{turb} are the collision velocity induced by Brownian motion, radial drift, azimuthal drift, vertical settling, and disk turbulence, respectively. We evaluate these components using the prescription described in Okuzumi et al. (2012).

2.3. Initial and outer boundary condition

We assume that the initial dust-to-gas mass ratio in the disk is $f_{\text{dg,ISM}} = 1/100$, and that the dust surface density profile is initially given as $\Sigma_{\text{dust}} = f_{\text{dg,ISM}} \Sigma_{\text{gas}}$. We also assume that the initial dust size is constant in the disk and given as $a_{\text{dust,init}} = 1 f^{-1/3} \mu\text{m}$, where f is the filling factor. For consistency, we introduced the factor $f^{-1/3}$ to the internal density $\rho_{\text{int}} \propto a^3 f$.

To mimic mass accretion from the envelope, the mass flux at the outer boundary is kept constant during the simulation. The dust-to-gas mass ratio and dust size at the outer boundary are set as $f_{\text{dg,ISM}}$ and $a_{\text{dust,init}}$, respectively. Thus, $\dot{M}_{\text{dust}} = f_{\text{dg,ISM}} \dot{M}_{\text{gas}}$ at the boundary. With this treatment, we implicitly assume that the mass loading from the envelope primarily occurs at the disk edge.

Mass loading from the disk edge well describes realistic envelope-to-disk mass accretion. Previous studies employing MHD simulations have reported the formation of pseudo-disks and outflow (e.g., Allen et al. 2003; Machida et al. 2011; Tsukamoto et al. 2015b). A pseudo-disk is a flattened disk-like structure that forms around a disk and connects to the disk edge. Because mass accretion primarily occurs through the pseudo-disk, almost all of the gas accretes onto the disk edge. Furthermore, as the outflow has a large opening angle and sweeps up gas residing above the disk (Machida et al. 2008; Price et al. 2012), the gas cannot accrete from the vertical direction. Based on these considerations, we assume that the gas and dust mass are primarily loaded from the disk edge.

2.4. Opacity of dust aggregate

To estimate the radiative flux of dust thermal emission from the simulated dust disk, we calculate the absorption opacity of the dust aggregates, $\kappa_{\text{d},\lambda}$ using the analytic formula given by Kataoka et al. (2014). The dust monomers are assumed to be composed of silicate, carbonaceous materials, and water ice. The mass fraction abundances are identical to those adopted by Pollack et al. (1994), $\zeta_{\text{silicate}} : \zeta_{\text{carbon}} : \zeta_{\text{ice}} = 2.64 : 3.53 : 5.55$. We employ the values for the refractive indices of astronomical silicate, amorphous carbon, and water ice given by Weingartner & Draine (2001), Zubko et al. (1996), and water ice given by Warren (1984), respectively. The effective monomer refractive index is calculated using the Bruggeman mixing rule.

As we consider porous dust aggregates in this paper, it is necessary to know their opacity. We can regard a porous aggregate as a mixture of monomers and vacuum, and effective medium theory can be applied in order to obtain the effective refractive index. This is calculated using the Maxwell-Garnett rule (for details, see Kataoka et al. 2014). We assume that the dust size distribution obeys a power law $dn/da \propto a^{-2.5}$ with cut-off radii of $a_{\text{min}} = a_{\text{dust,init}}$ and $a_{\text{max}} = a_{\text{dust}}$. This power law is slightly shallower than that estimated for the ISM $dn/da \propto a^{-3.5}$, or $q = 3.5$ (Mathis et al. 1977), because, as discussed in Miyake & Nakagawa (1993), a smaller q is expected when the coagulation process dominates the fragmentation process that is true in the situation we consider in this paper. The shallower size distribution is also expected to explain the observed small value of the opacity spectral index β Ricci et al. (2010b).

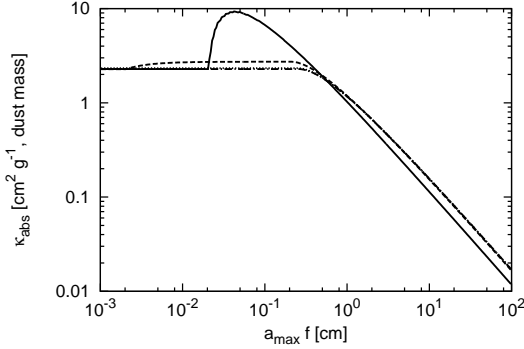


FIG. 1.— Absorption opacity at $\lambda = 1.3$ mm as a function of the product of the maximum dust radius and the filling factor, $a_{\max}f$. The solid, dashed, dotted, and dashed-dotted lines show the opacity for $f = 1, 10^{-1}, 10^{-2}$, and 10^{-3} , respectively.

Figure 1 shows the dust absorption opacity at $\lambda = 1.3$ mm (which corresponds to ALMA Band 6) as a function of the product of maximum dust size and filling factor, $a_{\max}f$. To obtain the opacity for this figure, we assume that $a_{\min} = 0.1 \mu\text{m}$. As noted in Kataoka et al. (2014), the filling factor and the dust size degenerate, thus, the dust opacity is identical for $af \ll 1$ cm and $af \gg 1$ cm. However, the opacity is enhanced at $10^{-2} \text{ cm} \lesssim a_{\max} \lesssim 1$ cm in the compact case ($f = 1$). This enhancement causes overestimation of the dust mass based on the dust thermal emission (see figure 9). We expect, however, that this enhancement is not important in a realistic situation because the realistic dust aggregates may have $f \lesssim 10^{-1}$, as suggested by observation of comets (A’Hearn et al. 2005; Pätzold et al. 2016), as well as by recent theoretical studies on dust coagulation incorporating porosity evolution (Ormel et al. 2007; Okuzumi et al. 2012). The value of the opacity is consistent with previous works (Ricci et al. 2010b; Okuzumi et al. 2016).

2.5. Parameters and Models

In this paper, as parameters, we choose the mass accretion rate \dot{M}_{gas} , radius of the disk r_{disk} , the mass of the central star M_{star} , and the filling factor f . Table 1 lists the model names and parameter choices that are investigated in §3. Furthermore, to derive the empirical formula shown in equation (37), we executed a total of 144 simulations.

3. RESULTS

3.1. Results from the fiducial model

In this subsection, we describe the results obtained from our chosen fiducial model, M1Mdot37r100f1. The dependence on the model parameters is discussed in subsequent subsections.

3.1.1. Timescale for settling into the steady state

In figure 2, we show the time evolution of the dust structure. As shown in the top left panel, the dust surface density quickly decreases owing to rapid dust growth and subsequent radial migration. The dust disk settles into the steady state at $t \sim 0.15$ Myr. As a result, the structures at $t = 0.15$ Myr and $t = 1.0$ Myr (at the end of the simulation) are identical. The steady-state settling

is particularly clear in terms of \dot{M}_{dust} (top-right panel), which becomes radially constant at $t \sim 0.15$ Myr. The timescale for steady-state settling can be estimated from the timescale when the dust grows to the size at which radial drift begins at the disk edge, which is estimated as (Okuzumi et al. 2012)

$$t_{\text{grow}} \equiv \left(\frac{d \ln m_{\text{dust}}}{dt} \right)^{-1} = \frac{4\sqrt{2\pi}}{3} \frac{H_{\text{dust}} \rho_{\text{int}} a}{\Delta v \Sigma_{\text{dust}}} \\ \sim 3.4 \times 10^4 \left(\frac{M_{\text{star}}}{M_{\odot}} \right)^{-1/2} \left(\frac{r}{100 \text{ AU}} \right)^{3/2} \text{ years}, \quad (22)$$

where we assume the gas disk structure of equations (8) and (9), $H_{\text{dust}} = (\text{St}/\alpha)^{-1/2} H_{\text{gas}}$, $\Delta v = \sqrt{\alpha c_s^2 \text{St}}$, and the Epstein drag law. We also assume that the dust-to-gas mass ratio at the edge of the disk is 1/100. This timescale corresponds to the mass doubling time and our simulation results show that the timescale for dust growth to cm-sized dust is slightly longer ($\sim 10^5$ yr) than this estimate. The dust growth timescale is shorter than the lifetimes of Class 0/I YSOs, which are typically 0.5 Myr (Evans et al. 2009; Williams & Cieza 2011). Therefore, it is expected that the dust structure in the Class 0/I phase can be described by the steady-state solution for the dust disk. The analytic solutions for the steady-state structure are discussed in detail in Appendix A.

3.1.2. Steady-state structure of dust disk

Hereafter, we focus on the steady-state structure of the dust disk (shown as dotted and dashed-dotted lines). The top-left panel of figure 2 shows the dust surface density. The dust surface density at the outer region, $r \gtrsim 80$ AU, is identical to its initial value because the dust particles are small and move with the gas advection. As a result, the initial dust-to-gas mass ratio is maintained in this region. Once the dust particles grow and the dust drift velocity overtakes the gas advection velocity, inward drifting of the dust particles begins. In our fiducial model, the radius at which the radial drift begins is $r_{\text{drift}} \sim 80$ AU. For $r < r_{\text{drift}}$, the dust-to-gas mass ratio decreases from its initial values owing to the faster radial motion of the dust particles. The dust surface density for $20 \text{ AU} \lesssim r \lesssim 80 \text{ AU}$ asymptotically obeys the power law $\Sigma_{\text{dust}} \propto r^{-31/28}$, which is the asymptotic steady-state solution (equation (A11), dotted black line).

r_{drift} can be estimated by considering the radius at which the gas advection velocity is equal to the dust drift velocity

$$v_{r,\text{gas}} = v_{r,\text{dust}} \sim 2\text{St}\eta v_K, \quad (23)$$

where we assume $\text{St} \ll 1$. By assuming the gas disk structure of equations (8) – (9), we obtain

$$r_{\text{drift}} = 2.2 \times 10^2 \left(\frac{\text{St}}{10^{-2}} \right)^{14/9} \left(\frac{\dot{M}_{\text{gas}}}{10^{-7} M_{\odot} \text{ yr}^{-1}} \right)^{-14/9} \text{ AU}. \quad (24)$$

If we assume $\text{St} = 0.01 - 0.02$, as is suggested by the bottom panel, and $\dot{M}_{\text{gas}} = 3 \times 10^{-7} M_{\odot} \text{ yr}^{-1}$, then $r_{\text{drift}} = 40 - 120$ AU. This estimate crudely explains our numerical results.

As the dust migrates inwards, a_{dust} exceeds the mean

TABLE 1
MODELS INVESTIGATED IN §3 AND THEIR PARAMETERS. NOTE THAT WE EXECUTE 144 SIMULATIONS IN TOTAL IN ORDER TO DERIVE OUR EMPIRICAL FORMULA, SHOWN IN EQUATION (37) AND MOST OF THEM ARE NOT SHOWN IN THIS TABLE.

Model name	Stellar mass (M_\odot)	Gas accretion rate ($M_\odot \text{ yr}^{-1}$)	Disk radius (AU)	Filling factor	Comment
M1Mdot37r100f1	1	3×10^{-7}	100	10^{-1}	fiducial model
M05Mdot37r100f1	0.5	3×10^{-7}	100	10^{-1}	
M2Mdot37r100f1	2	3×10^{-7}	100	10^{-1}	
M1Mdot36r100f1	1	3×10^{-6}	100	10^{-1}	
M1Mdot16r100f1	1	1×10^{-6}	100	10^{-1}	
M1Mdot17r100f1	1	1×10^{-7}	100	10^{-1}	
M1Mdot37r50f1	1	3×10^{-7}	50	10^{-1}	
M1Mdot37r200f1	1	3×10^{-7}	200	10^{-1}	
M1Mdot37r100f0	1	3×10^{-7}	100	10^0	
M1Mdot37r100f2	1	3×10^{-7}	100	10^{-2}	
M1Mdot37r100f4	1	3×10^{-7}	100	10^{-4}	
M2Mdot37r100f4	2	3×10^{-7}	100	10^{-4}	
M2Mdot37r100f5	2	3×10^{-7}	100	10^{-5}	
M1Mdot37r100f5	1	3×10^{-7}	100	10^{-5}	

free path and the drag law changes to the Stokes' law at a certain radius r_{Stokes} . The change in the drag law is identified by the change in the profile at $r \sim 10$ AU. In the region of the Stoke regime, Σ_{dust} is an increasing function of r . Through the analytic discussion in Appendix A, we can show that the dust surface density asymptotically obeys the power law $\Sigma_{\text{dust}} \propto r^{19/42}$ when $\Delta v = \sqrt{\alpha c_s^2 \text{St}}$ and $H_{\text{dust}} = (\text{St}/\alpha)^{-1/2} H_{\text{gas}}$, and we can confirm the positive power law of Σ_{dust} . However, because of the narrow Stokes drag region in the disk, the structure does not converge into the asymptotic solution. Rather, it is steeper than the solution. r_{Stokes} can be estimated from the condition

$$a_{\text{dust}} = \frac{9}{4} \lambda_{\text{mfp}}. \quad (25)$$

From the gas disk structure of equations (8) and (9), the radius is given as,

$$r_{\text{Stokes}} = 9.6 \left(\frac{M_{\text{star}}}{M_\odot} \right)^{7/22} \left(\frac{\text{St}}{0.01} \right)^{7/33} \left(\frac{\rho_{\text{int}}}{0.1 \text{ g cm}^{-3}} \right)^{-7/33} \text{ AU}. \quad (26)$$

This agrees well with our results.

The middle-left panel of figure 2 shows the collision velocity of the dust particles. In the steady state $\Delta v \lesssim 15 \text{ m s}^{-1}$ at $r > 10$ AU, and asymptotically obeys the power law $\Delta v \propto r^{1/8}$ in $10 \text{ AU} \lesssim r \lesssim 80 \text{ AU}$ (equation (A15), dotted black line). The collision velocity is significantly smaller than the threshold velocity v_{th} for collisional fragmentation. Simulations of aggregate collisions by Wada et al. (2013) showed that $v_{\text{th}} \sim 80 \text{ m s}^{-1}$ for aggregates composed of $0.1 \mu\text{m}$ sized icy monomer grains, and we chose $v_{\text{th}} = 80 \text{ m s}^{-1}$ (black solid line). Furthermore, as we noted in section §2.1.3, the collision velocity in our simulations is slightly overestimated. Thus, we conclude that collisional fragmentation does not play a major role in our model.

As shown in the middle-right panel of figure 2, a_{dust} quickly increases and becomes greater than 1 cm in $r \lesssim$

70 AU, asymptotically obeying the power law $a_{\text{dust}} \propto r^{-47/28}$. Figure 2 shows that the dust particles migrate in the form of centimeter-scale particles or "pebbles" in the disk during the Class 0/I phase. Because the amount of dust that passes through the disk is quite large in the Class 0/I phase (approximately 1 % of the central-star mass), the pebble accretion scenario for planet formation (Ormel & Klahr 2010; Lambrechts & Johansen 2012, 2014) seems to be preferred in the Class 0/I phase compared to the Class II phase, in which dust depletion at the disk outer edge limits the embryo growth by pebble accretion (Ida et al. 2016).

3.1.3. Reduction of the dust mass and thermal emission

As implied from the top-left panel of figure 2, the total dust mass in the steady disk M_{dust} systematically decreases from the disk with the ISM dust-to-gas mass ratio $f_{\text{dg,ISM}} = 1/100$. We define the reduction rate of dust mass in the disk owing to the dust depletion μ_{M} as

$$\mu_{\text{M}} \equiv \frac{M_{\text{dust,steady}}}{f_{\text{dg,ISM}} M_{\text{gas}}}. \quad (27)$$

Here, $M_{\text{dust,steady}} \equiv \int_{r_{\text{min}}}^{r_{\text{max}}} \Sigma_{\text{dust,steady}}(r) 2\pi r dr$ and $M_{\text{gas}} \equiv \int_{r_{\text{min}}}^{r_{\text{max}}} \Sigma_{\text{gas}}(r) 2\pi r dr$ where $\Sigma_{\text{dust,steady}}$ is the steady-state dust surface density. μ_{M} is the ratio of the dust mass in the steady-state disk to that in the disk with $f_{\text{dg,ISM}}$. (or the initial dust disk in our simulation). By numerically integrating equation (27) taking the inner and outer cut-off radius as $r_{\text{min}} = 10 \text{ AU}$ and $r_{\text{max}} = 100 \text{ AU}$, we obtain

$$\mu_{\text{M}} = 0.34, \quad (28)$$

for our fiducial model. Therefore, the dust-to-gas mass ratio of the disk for our fiducial model becomes approximately

$$f_{\text{dg,steady}} \equiv \mu_{\text{M}} f_{\text{dg,ISM}} \sim 1/300, \quad (29)$$

and is smaller than the value for the ISM.

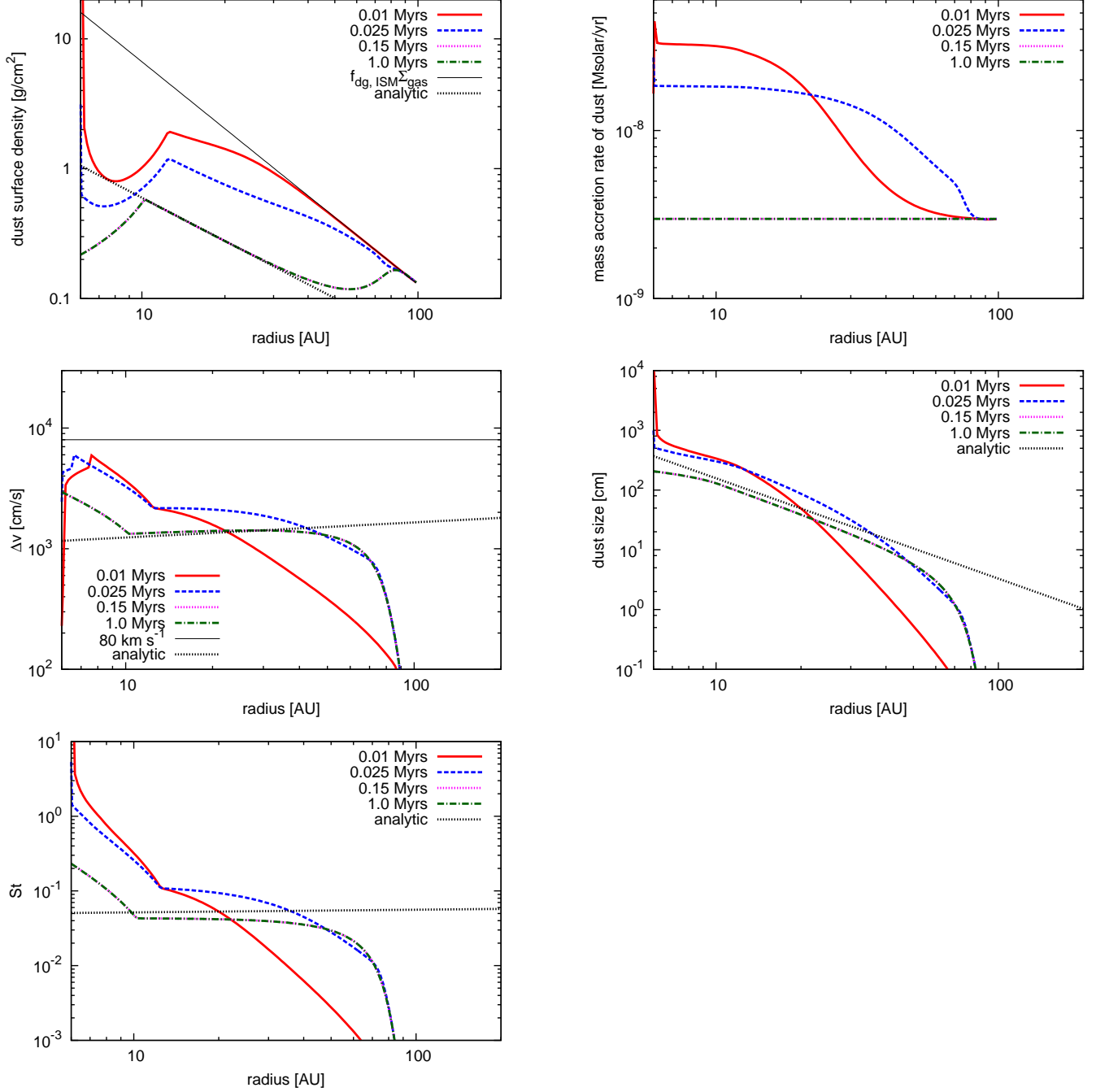


FIG. 2.— Time evolution of the radial profile of dust density, mass accretion rate, collision velocity, dust size, and Stokes number of our fiducial model, M1Mdot37r100f1. The red solid, blue dashed, magenta dotted, and green dashed-dotted lines show the profiles at $t = 0.01, 0.025, 0.15,$ and 1.0 Myr, respectively. The black solid lines in the surface density and in the collision velocity plots show $f_{\text{dg,ISM}}\Sigma_{\text{gas}}$ and the threshold velocity $v_{\text{th}} = 80 \text{ m s}^{-1}$, respectively. The black dashed lines show the analytic steady-state solutions under the condition where $\Delta v = \sqrt{2\alpha_c^2 \text{St}}$, $H_{\text{dust}} = (\text{St}/\alpha)^{-1/2} H_{\text{gas}}$, and the Epstein law is followed (equations (A11)– (A15)).

Furthermore, as dust growth reduces its opacity, the apparent mass of the dust disk that is estimated from the dust thermal emission assuming the opacity of micron-sized dust becomes smaller than M_{dust} . In this paper, we consider the dust thermal emission at $\lambda = 1.3\text{mm}$ which corresponds to ALMA Band 6. The radiative flux from

the dust disk in the steady state can be calculated as

$$F_{\text{steady},1.3\text{mm}} = \frac{4\pi}{D^2} \int_{r_{\text{min}}}^{r_{\text{max}}} \{[1 - \exp(\tau_{\text{steady},1.3\text{mm}}(r))] B_{1.3\text{mm}}(T(r))\} 2\pi r dr \quad (31)$$

where

$$\tau_{\text{steady},1.3\text{mm}}(r) = \kappa_{1.3\text{mm}}(a_{\text{dust,steady}}(r)) \Sigma_{\text{dust,steady}}(r) \quad (32)$$

and $\kappa_{1.3\text{mm}}$, $a_{\text{dust,steady}}$, $B_{1.3\text{mm}}$ and D are the dust

opacity at $\lambda = 1.3\text{mm}$, the dust radius in the steady state, the Planck function at $\lambda = 1.3\text{mm}$, and the distance of the source, respectively. To calculate the dust opacity, we set $a_{\min} = a_{\text{init}}$, $a_{\max} = a_{\text{dust}}$. Because the disk mass is often estimated from the dust thermal emission by assuming micron-sized dust opacity, ISM dust-to-gas mass ratio, and that dust disk is optically thin, we can define the "effective" reduction rate of the dust mass owing to dust depletion and opacity reduction μ_F as satisfying

$$\mu_F = \frac{F_{\text{steady}, 1.3\text{mm}}}{F_{\text{ISM}, 1.3\text{mm}}}. \quad (32)$$

where $F_{\text{ISM}, 1.3\text{mm}}$ is the radiative flux defined as

$$F_{\text{ISM}, 1.3\text{mm}} \equiv \frac{4\pi}{D^2} \int_{r_{\min}}^{r_{\max}} \{\kappa_{1.3\text{mm}}(a_{\text{ISM}})(f_{\text{dg}, \text{ISM}} \Sigma_{\text{gas}}(r)) B_{1.3\text{mm}}(T(r))\} 2\pi r dr, \quad (33)$$

where we assume the typical dust size of the ISM a_{ISM} to be $a_{\text{ISM}} = 0.1\mu\text{m}$.

In the steady state of our fiducial model,

$$\mu_F = 0.17. \quad (34)$$

Thus, the "effective" dust-to-gas mass ratio for our fiducial model is calculated as

$$f_{\text{dg}, \text{eff}} \equiv \mu_F f_{\text{dg}, \text{ISM}} \sim 1/500. \quad (35)$$

The reduction of dust thermal emission causes underestimation of M_{gas} because the gas mass is often estimated by assuming $f_{\text{dg}, \text{ISM}}$ and the opacity of micron-sized dust. The apparent gas disk mass M_{app} is calculated as

$$M_{\text{app}} \equiv \mu_F M_{\text{gas}}. \quad (36)$$

In our fiducial model, the gas disk mass is $M_{\text{gas}} = \int \Sigma_{\text{gas}} 2\pi r dr = 0.16 M_{\odot}$ where the inner and outer cut-off radii are chosen to be $r_{\text{in}} = 10 \text{ AU}$ and $r_{\text{out}} = r_{\text{disk}} = 100 \text{ AU}$, respectively. The apparent gas disk mass estimated from the dust thermal emission is $M_{\text{app}} = 0.027 M_{\odot}$ and is apparently gravitationally stable. Thus, even when a gravitationally unstable disk exists in a Class I YSO, it appears to be gravitationally stable. Note that M_{app} is consistent with the observed disk mass $M_{\text{gas}, \text{obs}}$ of Class I YSOs in the range $0.01 M_{\odot} < M_{\text{gas}, \text{obs}} < 0.1 M_{\odot}$ (Andrews & Williams 2007; Jørgensen et al. 2009).

3.2. Parameter study

In this subsection, we investigate how the steady-state structure and apparent disk mass depend on the model parameters. The parameters we consider in this subsection are the mass accretion rate onto the disk \dot{M}_{gas} , the filling factor of the dust aggregate f , the radius of the disk r_{disk} , and the central-star mass M_{star} . In the models considered in this section, the steady state is reached within 0.2 Myr and it is expected that the dust disk is in its steady state in the Class I phase. Therefore, we focus on the dependence of the steady-state structure on the parameters.

3.2.1. Dependence on mass accretion rate

In the top-left panel of figure 3, we show the surface density profiles of the the steady-state dust disk for various mass accretion rate ($\dot{M}_{\text{gas}} = 1 \times 10^{-7}, 3 \times 10^{-7}, 1 \times$

$10^{-6}, 3 \times 10^{-6} M_{\odot} \text{ yr}^{-1}$). The surface density of the dust for $r_{\text{Stokes}} < r < r_{\text{drift}}$ is an increasing function of \dot{M}_{gas} . It depends on the mass accretion rate as $\Sigma_{\text{dust}} \propto \dot{M}_{\text{gas}}^{1/2}$ (see equation (A11)). Thus, as the mass accretion decreases, M_{app} decreases although the actual gas mass M_{gas} is independent of \dot{M}_{gas} (equation (8)).

The top-right panel of figure 3 shows the collision velocity. Even with the relatively large mass accretion rate, ($\dot{M}_{\text{gas}} = 3 \times 10^{-6} M_{\odot} \text{ yr}^{-1}$), the collision velocity is smaller than the threshold velocity ($v_{\text{th}} = 80 \text{ m s}^{-1}$) for $r \gtrsim 10 \text{ AU}$, and our assumption of perfect sticking is still justified. However, if we consider a slightly larger mass accretion rate, e.g., $\dot{M}_{\text{gas}} = 10^{-5} M_{\odot} \text{ yr}^{-1}$, which may occur in some Class 0/I YSOs, collisional fragmentation plays a dominant role in determining the dust structure. Note also that the threshold velocity adopted in this paper is derived with $0.1 \mu\text{m}$ sized monomer and it may decrease if the monomer size is large. If this is the case, the collisional fragmentation becomes dominant with smaller mass accretion rate. The collision velocity exhibits the following dependence on the mass accretion rate: $\Delta v \propto (\alpha \text{St})^{1/2} \propto \dot{M}_{\text{gas}}^{3/4}$ (see, (9) and (A12)).

The bottom-left panel of figure 3 shows the radial profile of dust size. In the outer part of the disk ($r \gtrsim 80 \text{ AU} \sim r_{\text{drift}}$), the dust size increases as the accretion rate decreases owing to the small gas advection velocity in the small mass accretion models. Because of the small advection velocity, the dust particles can remain in the outer region for a long period of time and have sufficient time to grow to a larger size. On the other hand, in the inner part of the disk ($r_{\text{Stokes}} < r < r_{\text{drift}}$), the dust size increases as $a_{\text{dust}} \propto \dot{M}_{\text{gas}}^{1/2}$ (equation (A13)).

In the left panel of figure 4, we show μ_M and μ_F for various mass accretion rates. As pointed out above, μ_F indicates the effective reduction rate of the gas mass. Both μ_M and μ_F are increasing functions of the mass accretion rate. The dashed line shows our empirical formula for μ_F , equation (37), which indicates that $\mu_F \propto \dot{M}_{\text{gas}}^{0.17}$.

The right panel of figure 4 shows the apparent mass of the gas disk as a function of the mass accretion rate calculated according to $M_{\text{app}} = \mu_F M_{\text{gas}}$. The black line shows the actual gas mass in the disk, $M_{\text{gas}} = 0.16 M_{\odot}$. Because the mass of a gravitationally unstable disk does not depend on the mass accretion rate, the actual gas disk mass is constant. In all cases shown in the figure, the apparent mass is within the mass range suggested by observations of Class I YSOs, $0.01 M_{\odot} \lesssim M_{\text{gas}, \text{obs}} \lesssim 0.1 M_{\odot}$.

3.2.2. Dependence on central-star mass

In the top-left panel of figure 5, we show the surface density profile of dust for various central-star masses ($M_{\star} = 0.5, 1.0, 2.0 M_{\odot}$). Interestingly, once radial drift begins, Σ_{dust} converges to the same steady-state solution for $r_{\text{Stokes}} < r < r_{\text{drift}}$, independent of the central-star mass, which can be understood as follows. Because we consider a gravitationally unstable disk, $\Sigma_{\text{gas}} \propto \Omega \propto M_{\text{star}}^{1/2}$. From equation (A12), by assuming $\Delta v = \sqrt{\alpha c_s^2 \text{St}}$, $H_{\text{dust}} = (\text{St}/\alpha)^{-1/2} H_{\text{gas}}$, and Epstein drag, we can find $t_{\text{coll}}/t_{\text{drift}} \propto \Omega \Sigma_{\text{gas}} \text{St}^{-2} \propto M_{\text{star}}^0$ and hence, $\text{St} \propto (\Omega \Sigma_{\text{gas}})^{1/2} \propto M_{\text{star}}^{1/2}$. Then, from (A3),

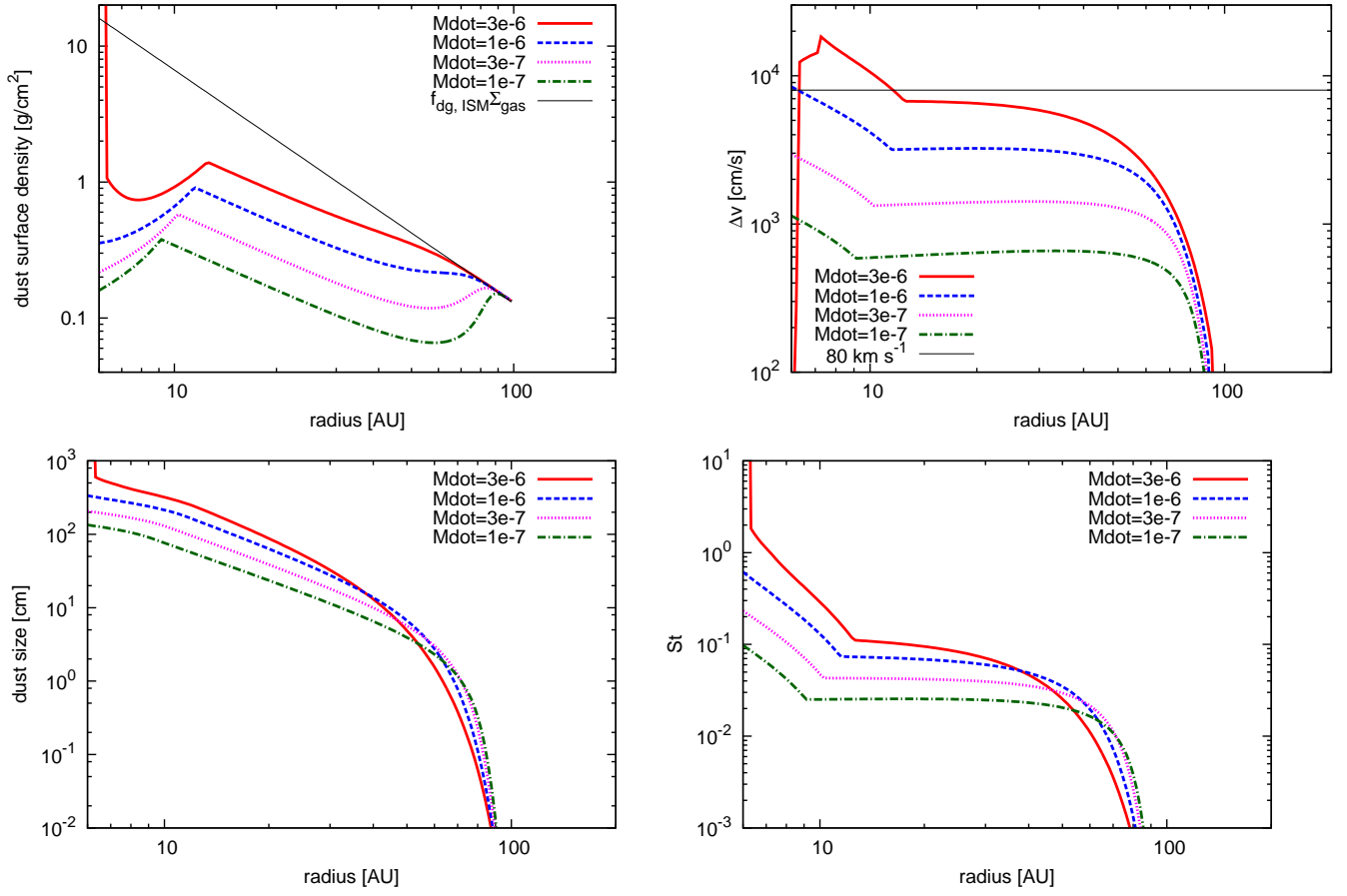


FIG. 3.— Radial profiles of dust surface density (top left), collision velocity (top right), dust size (bottom left), and Stokes number (bottom right) in the steady state (at $t = 0.2 \text{ Myr}$) for various mass accretion rates. The red solid, blue dashed, magenta dotted, and green dashed-dotted lines show the profile of M1Mdot36r100f1, M1Mdot16r100f1, M1Mdot37r100f1, and M1Mdot17r100f1, respectively. The black solid lines in the surface density and in the collision velocity plots show $f_{\text{dg,ISM}} \Sigma_{\text{gas}}$ and the threshold velocity, respectively.

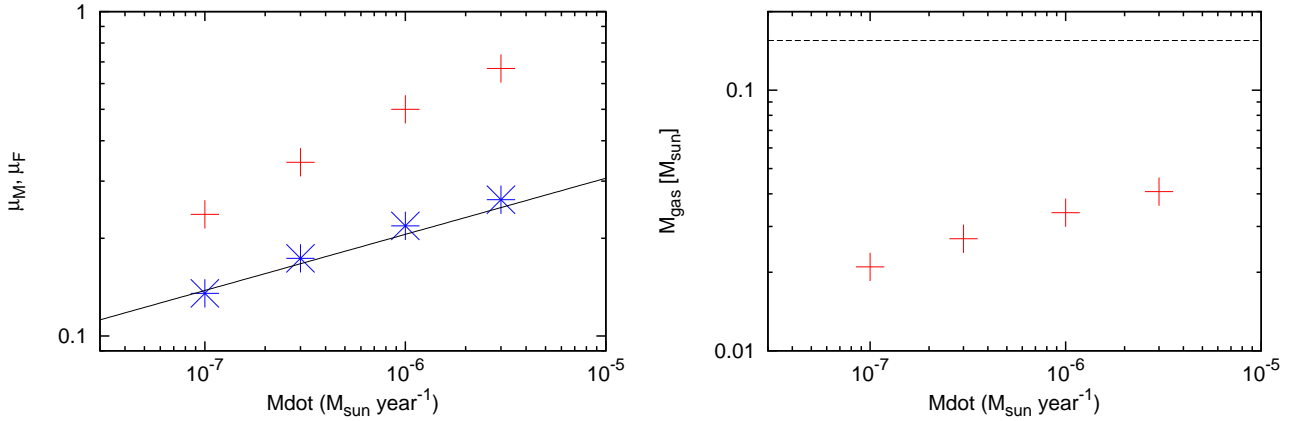


FIG. 4.— Left panel shows the ratio of the dust mass in the steady-state disk (at $t = 0.2 \text{ Myr}$) to that in the disk with ISM dust-to-gas mass ratio μ_M , and ratio of the radiative flux from the steady-state disk to that from the disk with ISM dust-to-gas mass ratio and micron-sized dust μ_F for various mass accretion rates. The red crosses and blue asterisks show μ_M and μ_F , respectively, of M1Mdot36r100f1, M1Mdot16r100f1, M1Mdot37r100f1, and M1Mdot17r100f1. The black solid line shows the empirical formula for μ_F , equation (37). The right panel shows the apparent mass M_{app} of the gas disk. The red crosses show M_{app} . Here, $M_{\text{app}} = \mu_F M_{\text{gas}}$, where $M_{\text{gas}} = \int \Sigma_{\text{gas}} 2\pi r dr$. The black dashed line shows the actual mass of the gas disk in the simulations, $M_{\text{gas}} = 0.16 M_{\odot}$.

$\Sigma_{\text{dust}} \propto (\eta v_K \text{St}) \propto (\text{St}/v_K)^{-1} \propto M_{\text{star}}^0$. Thus, the dust surface density in the Epstein regime is independent of the central-star mass. Because we use the fact that $\Sigma_{\text{gas}} \propto \Omega$, this is a unique feature of dust disks in gravitationally unstable gas disks.

r_{Stokes} increases with M_{star} because the mean free path depends on M_{star} as $\lambda_{\text{mfp}} \propto (\Sigma_{\text{gas}} \Omega)^{-1} \propto M_{\text{star}}^{-1}$. In addition, a_{dust} depends on M_{star} , as $a_{\text{dust}} \propto \text{St} \Sigma_{\text{gas}} \propto M_{\text{star}}$ at a certain r . As a result, the condition $a_{\text{dust}} = (9/4)\lambda_{\text{mfp}}$ is realized at a larger r , and r_{St} increases with increasing M_{star} .

As shown in the top right panel of figure 5, the collision velocity is also an increasing function of central-star mass, it scales as $\Delta v \propto \text{St}^{1/2} \propto M_{\text{star}}^{1/4}$ (equation (A15)). All models considered in this section satisfy the condition of $\Delta v < v_{\text{th}}$, and the collisional fragmentation does not change our results significantly.

In the left panel of figure 6, we show μ_{M} and μ_{F} as functions of the central-star mass. Both μ_{M} and μ_{F} are decreasing functions of the central-star mass. This dependence exists because, although Σ_{dust} converges to the same steady-state solution in the Epstein regime and the dust disk has roughly the same mass, the mass of the gas disk is an increasing function of the central-star mass as $M_{\text{gas}} \propto \Omega \propto M_{\text{star}}^{1/2}$. As a result, μ_{M} and μ_{F} decrease as the mass of the gas disk increases. Our empirical formula, equation (37), shows that $\mu_{\text{F}} \propto M_{\text{star}}^{-0.53}$, having a relatively strong dependence on the central-star mass.

The right panel of figure 6 shows the apparent mass, $\mu_{\text{F}} M_{\text{gas}}$, and the actual mass of the gas disk, M_{gas} , as functions of the central-star mass. The apparent mass has very weak dependence on the central-star mass. Although this result appears to contradict the results shown in the left panel of figure 6, there is no contradiction. As shown by the dashed line, the mass of a gas disk with constant Q value is an increasing function of M_{star} as $M_{\text{gas}} \propto M_{\text{star}}^{1/2}$. This positive dependence almost cancels the negative dependence of μ_{F} . The range of the apparent mass is again within the observed mass range from the dust thermal emission. The lack of correlation between the apparent mass and the central star mass stems primarily from the fact that the dust disk converges to the same steady-state solution in $r_{\text{Stokes}} \lesssim r \lesssim r_{\text{drift}}$ and has roughly the same total dust mass.

3.2.3. Dependence on the dust porosity

As shown in Okuzumi et al. (2012), dust aggregates may grow to highly porous aggregates with $\rho_{\text{int}} \ll 1 \text{ g cm}^{-3}$. Therefore, it is expected that the filling factor of dust aggregates in the protoplanetary disk has a small value ($f \ll 1$). In this section, we investigate how the dust profiles depend on the porosity. Note that we do not consider porosity evolution directly, rather, we treat it as a parameter.

Figure 7 shows the profiles of dust surface density, collision velocity, and Stokes number in the steady state for various filling factors. As shown in this figure, the dust surface density converges to the same steady-state solution for $r_{\text{Stokes}} < r < r_{\text{drift}}$. This is because, in the Epstein regime, $\text{St} \propto \rho_{\text{int}} a_{\text{dust}}$ and ρ_{int} and a_{dust} can be simultaneously eliminated from equation (A18) and the Stokes number does not depend on the filling factor. In addition, the dust surface density is solely determined by

the Stokes number.

r_{Stokes} increases as porosity decreases because a_{dust} is calculated from $a_{\text{dust}} = (2\Sigma_{\text{gas}} \text{St})/(\pi\rho_{\text{int}}) \propto f^{-1}$ and the mean free path does not depend on the internal density. The steady state in the Stokes regime, which is also determined by (A18), depends on ρ_{int} because we cannot eliminate the dust radius and internal density simultaneously from (A18) in the Stokes regime, and Σ_{dust} converges to the different steady solutions. In the model with $f = 10^{-4}$ (magenta dotted line), dusts grow quickly and enter the Stokes regime before the dust disk structure converges to the steady-state solution of the Epstein regime.

In the model with $f = 10^{-4}$, the surface density and Stokes number rapidly increase at $r \sim 20 \text{ AU}$, indicating planetesimal formation. Therefore, planetesimal formation is possible at $r \gtrsim 10 \text{ AU}$, if the filling factor decreases to $f \lesssim 10^{-4}$ in the gravitationally unstable disk. Note that the collision velocity is smaller than the threshold velocity ($v_{\text{th}} = 80 \text{ m s}^{-1}$) and our assumption of perfect sticking is valid in the models discussed in this subsection. Although porous dust aggregates can grow to large radii (in $f = 10^{-4}$ case, the radius becomes $a_{\text{dust}} \sim 10^4 \text{ cm}$ at $r \sim 20 \text{ AU}$), this growth does not significantly change the absorption opacity, because the opacity does not depend on the size a_{dust} , but on the product of the filling factor and the size, $a_{\text{dust}} f$ (Kataoka et al. 2013). In figure 8, we show $a_{\text{dust}} f$ in the steady state for various filling factors. $a_{\text{dust}} f$ converges to the same steady state, independent of f in the Epstein regime, because $a f \propto a \rho_{\text{int}} \propto \text{St}$, and St does not depend on the filling factor.

In the left panel of figure 9, we show μ_{M} and μ_{F} for various filling factors ($f = 1, 10^{-1}, 10^{-2}, 10^{-3}$, and 10^{-4}). For the calculation of the $f = 10^{-4}$ model, we set $r_{\text{min}} = r_P$ to limit complexity. The figure reveals a very weak dependence of μ_{M} on the filling factor. Although the dust is depleted in the inner region in the models with a small filling factor, its contribution to the total mass is not significant owing to the metric $2\pi r$ in the integral. Furthermore, in the $50 \text{ AU} \lesssim r \lesssim 80 \text{ AU}$ region, the surface densities for the models with small filling factor are slightly larger than those for the models with a large filling factor. As a result, μ_{M} is almost constant against changes in porosity.

On the other hand, μ_{F} exhibits a dependence on filling factor for $f \geq 10^{-1}$. From $f = 10^{-1}$ to $f = 1$, μ_{F} suddenly increases even though the dust mass is almost constant. This change is caused by the increase in absorption opacity. As shown in figure 1, the opacity for compact dust ($f = 1$) increases in the range $0.10^{-2} \text{ cm} \lesssim a_{\text{dust}} \lesssim 1 \text{ cm}$. Because the dust size in the $f = 1$ model enters this range in the outer region of the disk, $40 \text{ AU} \lesssim r \lesssim 80 \text{ AU}$, the thermal emission at $\lambda = 1.3 \text{ mm}$ from this region becomes larger than that with micron-sized dust. This causes an increase of μ_{F} in the $f = 1$ case. Note, however, that the compact case ($f = 1$) seems to be unlikely, both theoretically and observationally (A'Hearn et al. 2005; Pätzold et al. 2016; Ormel et al. 2007; Okuzumi et al. 2012). For $f < 10^{-1}$, μ_{F} is almost independent of f because the dust porosity mainly influences the inner structure of the disk and the contribution of the inner region to the radiative flux

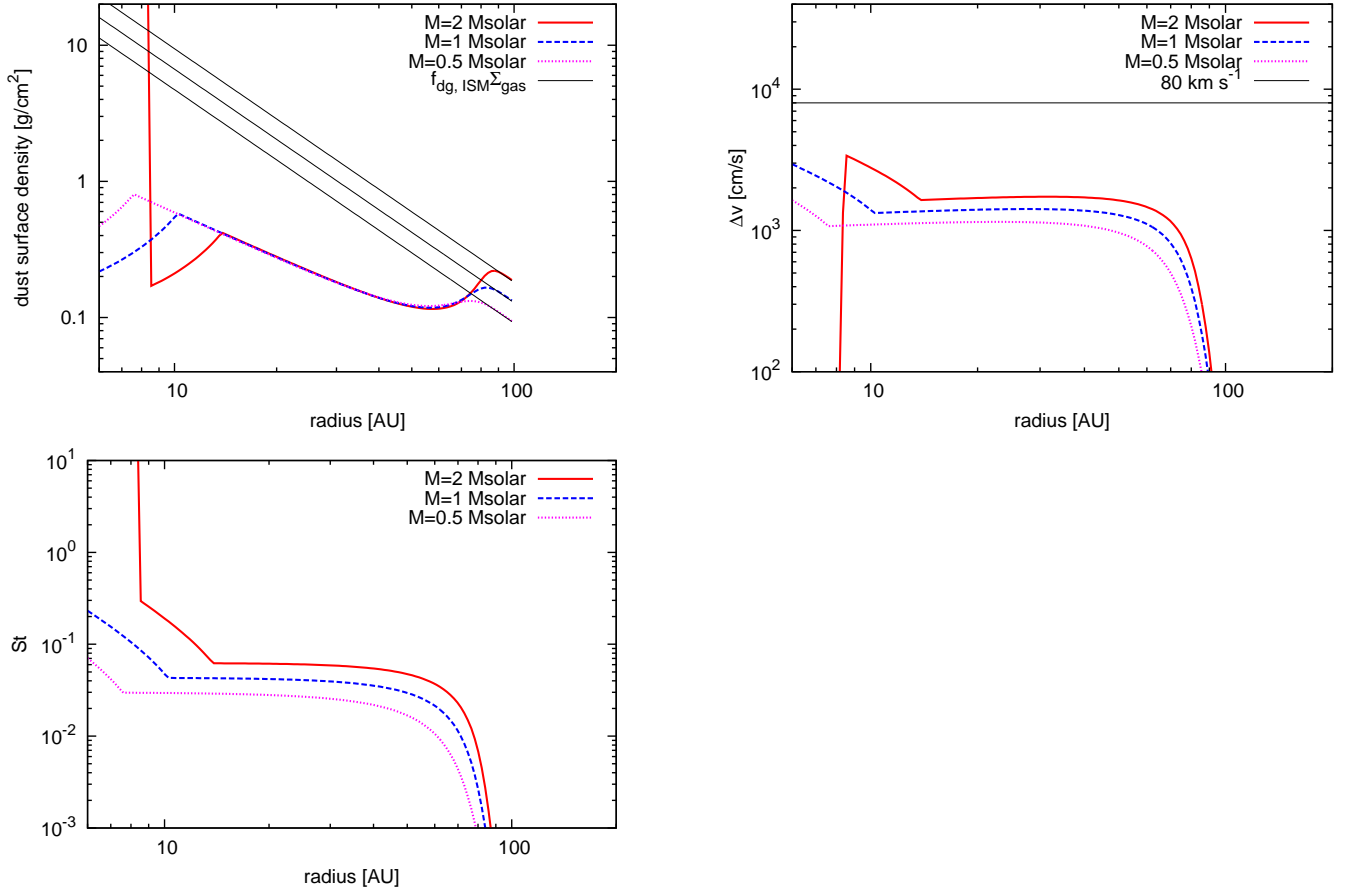


FIG. 5.— Radial profiles of dust surface density (top left), collision velocity (top right), and Stokes number (bottom) in the steady state (at $t = 0.2$ Myr) for various central-star masses. The red solid, blue dashed, and magenta dotted lines show the profile of M2Mdot37r100f1, M1Mdot37r100f1, and M05Mdot37r100f1, respectively. The black solid lines in the surface density and in the collision velocity plots show $f_{\text{dg,ISM}} \Sigma_{\text{gas}}$ and the threshold velocity, respectively.

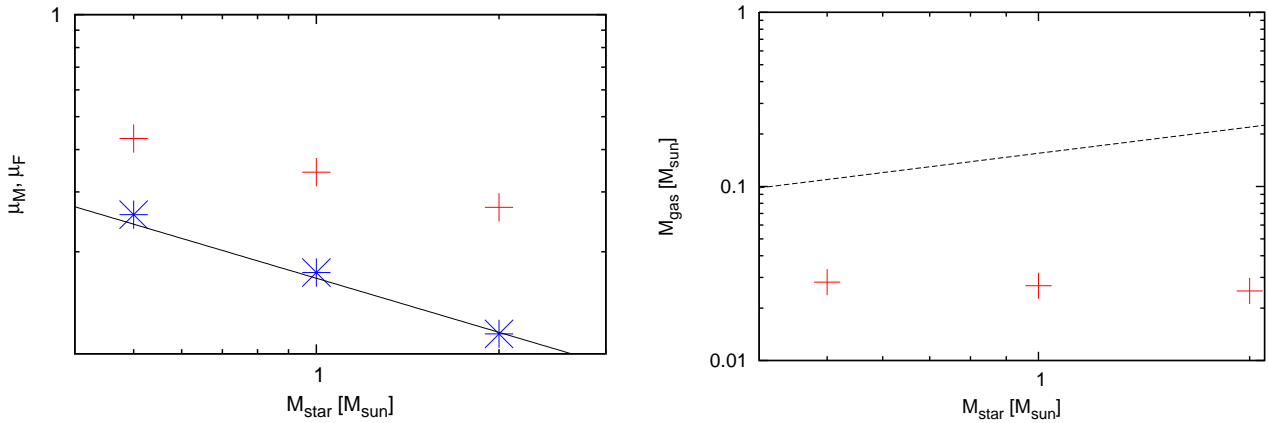


FIG. 6.— Left panel shows the ratio of the dust mass in the steady-state disk (at $t = 0.2$ Myr) to that in the disk with ISM dust-to-gas mass ratio μ_M , and ratio of the radiative flux from the steady-state disk to that from the disk with ISM dust-to-gas mass ratio and micron-sized dust μ_F for the various central-star masses. The red crosses and blue asterisks show μ_M and μ_F , respectively, of M2Mdot37r100f1, M1Mdot37r100f1, and M05Mdot37r100f1. The black solid line shows the empirical formula for μ_F , equation (37). The right panel shows the apparent mass M_{app} of the gas disk. The red crosses show M_{app} , which is calculated from $M_{\text{app}} = \mu_F M_{\text{gas}}$, where $M_{\text{gas}} = \int \Sigma_{\text{gas}} 2\pi r dr$. The black dashed line shows the actual mass of the gas disk in the simulations having $M_{\text{star}}^{1/2}$ dependency on the central-star mass.

is small owing to the opacity decrease by dust growth and the metric $2\pi r$ in the integral. As indicated by our empirical formula, equation (37), μ_F scales as $f^{0.0048}$ for $f \leq 10^{-1}$ and is almost independent of the filling factor.

In the left panel of figure 9, we show the apparent disk mass. The dependence of the disk mass on the porosity is so weak that it does not influence the apparent disk mass. Again, the apparent disk mass is within the range $0.01 M_\odot < M_{\text{app}} < 0.1 M_\odot$ as suggested by observations.

3.2.4. Dependence on the disk radius

In figure 10, we show the profiles of the dust surface density and dust size in the steady state for various disk radii ($r = 50, 100, \text{ and } 200 \text{ AU}$). Similar to previous cases, until the dust particles grow sufficiently for radial drift to begin, they move with the gas advection velocity. Once the dust radial drift begins, the dust surface density decreases from the initial value. Because the steady-state solution does not depend on the disk radius, all of the models converge to the same solution, both in the Epstein and the Stokes regimes, once the radial drift begins.

As shown in figure 11, μ_M is $0.3 < \mu_M < 0.4$, and the dust-to-gas mass ratio is less sensitive to the disk radius. On the other hand, the dependence of μ_F on the disk radius is relatively strong. This is because, in the disk with $r_{\text{disk}} = 50 \text{ AU}$, the dust size becomes $a_{\text{dust}} f > 1 \text{ cm}$ (see right panel of figure 10), and the dust opacity decreases over nearly the entire region of the disk. As shown in our empirical formula, equation (37), μ_F scales as $\mu_F \propto r_{\text{disk}}^{0.41}$. The apparent mass shown in the right panel of figure 11, increases rapidly as the disk radius increases because both M_{gas} and μ_F are increasing functions of the disk radius. Note, however, that even for a relatively large disk with $r = 200 \text{ AU}$, apparent mass is $0.05 M_\odot$ and within the range suggested by the observations.

3.3. Maximum radius for planetesimal formation

As pointed out by Okuzumi et al. (2012) and Kataoka et al. (2013), highly porous aggregates grow faster than radial drift and finally form planetesimals in the inner region of a disk for which Stokes drag law determines the dust stopping time. According to this scenario, the orbital radius within which planetesimals form r_P increases with the gas surface density (Okuzumi et al. 2012). On the other hand, a disk with a larger surface density than that of a gravitationally unstable disk cannot exist. Therefore, by investigating the parameter dependence of r_P in a gravitationally unstable disk, we can determine the maximum value for r_P .

As noted in §2.2, unlike the other results discussed in this paper, r_P inevitably depends on the initial conditions when we employ the radial drift velocity of equation (15). The r_P of a model using equation (15) indicates the maximum value for the parameter set of the model. On the other hand, r_P becomes independent of the initial condition when we employ the radial drift velocity of equation (17), and the r_P of a model using equation (17) indicates the orbital radius within which planetesimals form under a steady-state solution and is the minimum value for the parameter set. We first show the results obtained using equation (17) and then discuss the difference between the results with equation (15) and equation (17).

In the left panel of figure 12, we show the dust surface densities of the models in which planetesimals form for $r > 10 \text{ AU}$. A sudden increase in the dust surface density indicates planetesimal formation. r_{Stokes} and, therefore, r_P increase according to the increase in M_{star} and \dot{M}_{gas} , along with the decrease in Q_{crit} and f . Among these parameters, M_{star} and f strongly affect r_P . The maximum r_P is realized in the model with $M_{\text{star}} = 2 M_\odot$, $\dot{M}_{\text{gas}} = 3 \times 10^{-7} M_\odot \text{ yr}^{-1}$, $f = 10^{-5}$, and has a value of $r_P \sim 30 \text{ AU}$. On the other hand, if we consider the model with $M_{\text{star}} = 1 M_\odot$, $\dot{M}_{\text{gas}} = 3 \times 10^{-7} M_\odot \text{ yr}^{-1}$, $f = 10^{-5}$, the orbital radius within which planetesimals form is $r_P \sim 20 \text{ AU}$.

The right panel of figure 12 shows the profile of collision velocity. The collision velocity of all models considered in this section is smaller than the threshold velocity and neglecting the collisional fragmentation is still valid. Although r_P can increase with larger \dot{M}_{gas} , the collision velocity becomes too large and exceeds the threshold velocity. Thus, the collisional fragmentation cannot be avoided, and larger r_P may not be achieved by increasing \dot{M}_{gas} .

In figure 13, we compare r_P in the simulations with the equations (15) and (17). Thick lines indicate the results using the equation (15). As we discussed, r_P becomes large under equation (15). For example, in the model with $M_{\text{star}} = 1 M_\odot$, $\dot{M}_{\text{gas}} = 3 \times 10^{-7} M_\odot \text{ yr}^{-1}$, $f = 10^{-5}$, the orbital radius for planetesimal formation becomes $r_P \gtrsim 20 \text{ AU}$, which is approximately 10 AU larger than that under equation (17). This increase is caused by the large mass accretion rate and the large dust surface density at the beginning of the simulation. In reality, planetesimals may form between the two radii obtained using the equations (15) and (17). Summarizing the above discussion, we can conclude that planetesimal formation is possible at $r \sim 20 \text{ AU}$ in gravitationally unstable disks around protostars with $M_{\text{star}} = 1 M_\odot$. This is the theoretical maximum value of r_P according to the planetesimal formation mechanism suggested by Okuzumi et al. (2012) and Kataoka et al. (2013).

4. SUMMARY AND DISCUSSION

In this paper, we investigated the dust structure in a gravitationally unstable disk undergoing mass accretion from an envelope, envisioning the application of our findings to Class 0/I YSOs. We considered the growth and radial drift of dust particles with a single size approximation (Kornet et al. 2001; Birnstiel et al. 2012; Okuzumi et al. 2016; Sato et al. 2016). Comparing the dust thermal emission from a steady-state structure with that from a disk with ISM dust-to-gas mass ratio and micron-sized dust, we evaluated the apparent reduction rate of the gas disk mass estimated from the dust thermal emission at $\lambda = 1.3 \text{ mm}$, and showed that the disk mass is systematically underestimated.

We also investigated the orbital radius within which planetesimals form r_P in a gravitationally unstable disk, using the planetesimal formation mechanism suggested by Okuzumi et al. (2012). r_P of a gravitationally unstable disk is the theoretical maximum value because it increases with the gas surface density. Thus, we derived the maximum r_P for arbitrary disks.

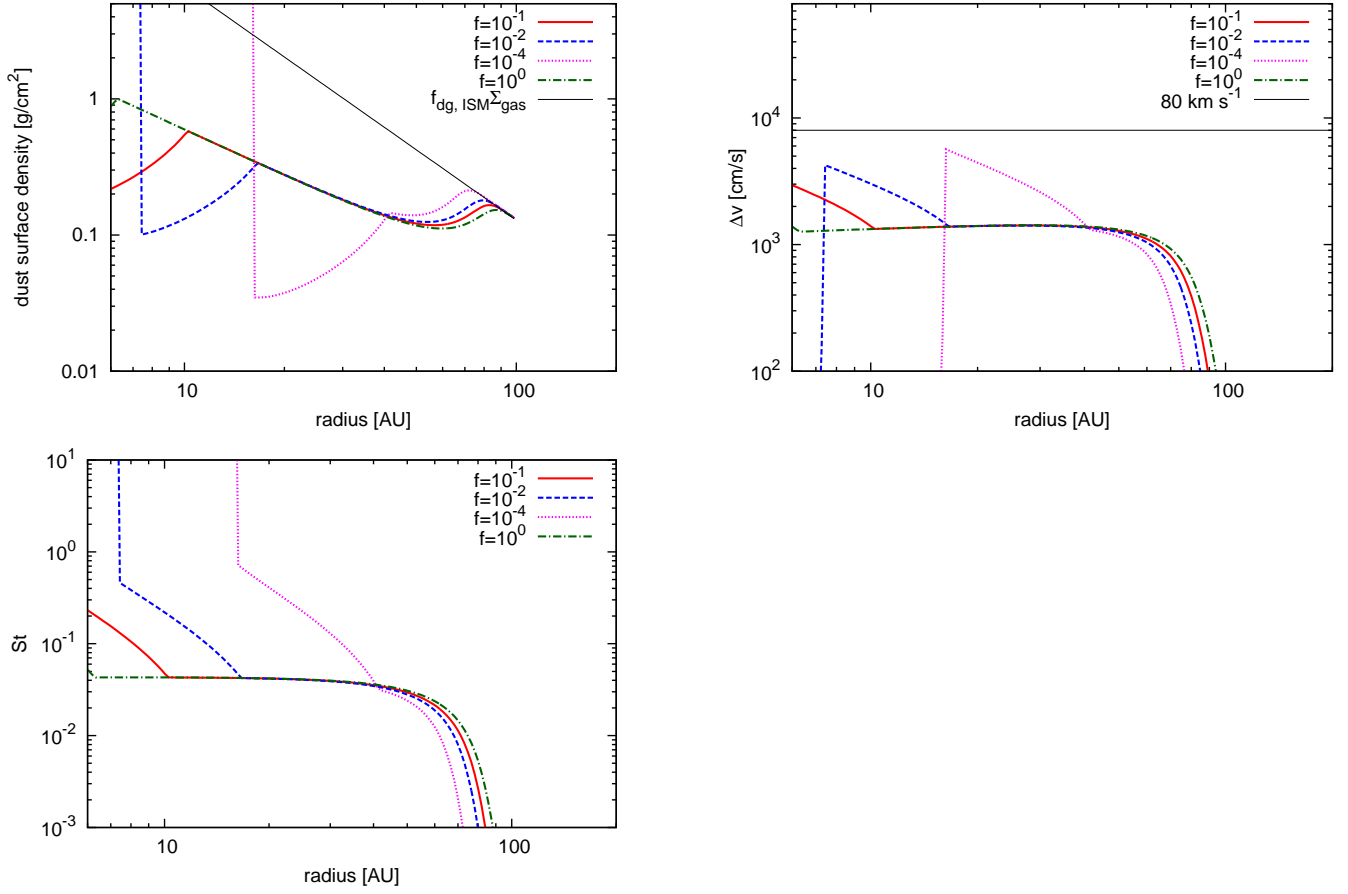


FIG. 7.— Radial profile of dust surface density (top left), collision velocity (top right), and Stokes number (bottom) in steady state (at $t = 0.2 \text{ Myr}$) for various filling factors. The red solid, blue dashed, magenta dotted, and green dashed-dotted lines show the profile of M1Mdot37r100f1, M1Mdot37r100f2, M1Mdot37r100f4, and M1Mdot37r100f0, respectively. The black solid lines in the top-left and top-right panels show $f_{\text{dg,ISM}}\Sigma_{\text{gas}}$ and the threshold velocity, respectively.

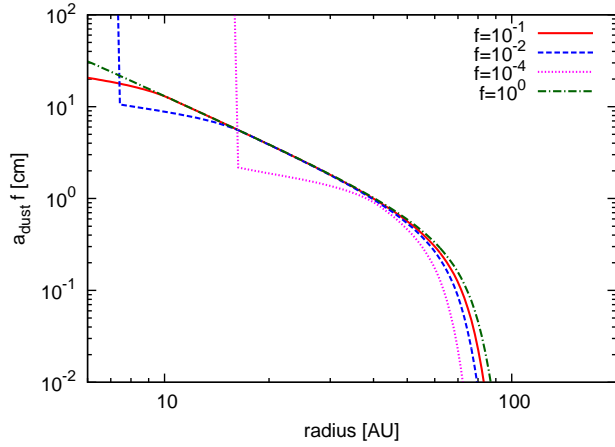


FIG. 8.— Radial profile of $a_{\text{dust}} f$ in steady state (at $t = 0.2 \text{ Myr}$) for various filling factors. The red solid, blue dashed, magenta dotted, and green dashed-dotted lines show the profiles of M1Mdot37r100f1, M1Mdot37r100f2, M1Mdot37r100f4, and M1Mdot37r100f0, respectively.

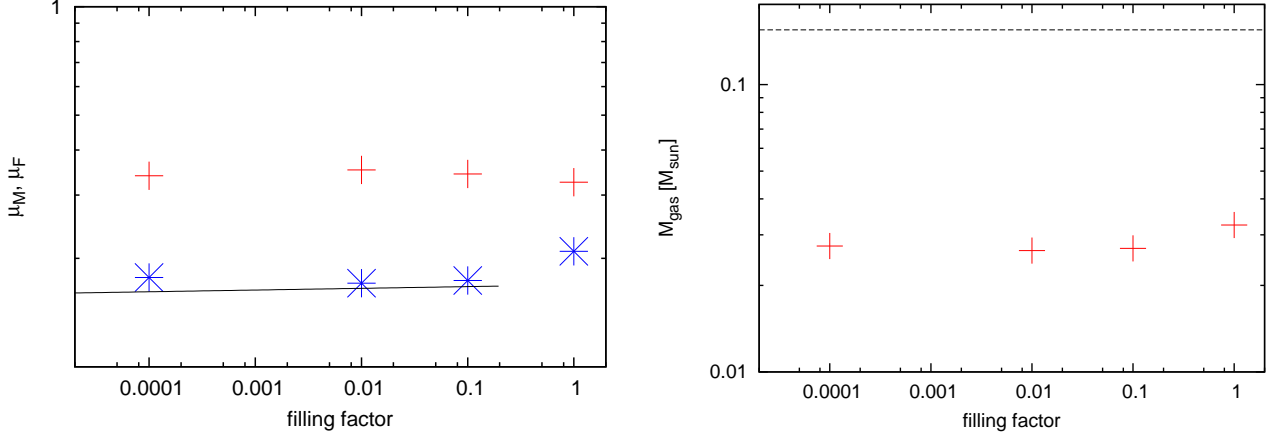


FIG. 9.— Left panel shows the ratio of dust mass in the steady-state disk (at $t = 0.2$ Myr) to that in a disk with the ISM dust-to-gas mass ratio μ_M , as well as the ratio of the radiative flux from the steady-state disk to that from a disk with the ISM dust-to-gas mass ratio and micron-sized dust μ_F for various filling factors. The red crosses and blue asterisks show μ_M and μ_F , respectively, of M1Mdot37r100f1, M1Mdot37r100f2, M1Mdot37r100f4, and M1Mdot37r100f0. The black solid line shows the empirical formula for μ_F , equation (37), which is applicable for $f \leq 10^{-1}$. The right panel shows the apparent mass M_{app} of the gas disk. The red crosses show M_{app} . The black dashed line shows the actual mass of the gas disk in the simulations, $M_{\text{gas}} = 0.16 M_{\odot}$.

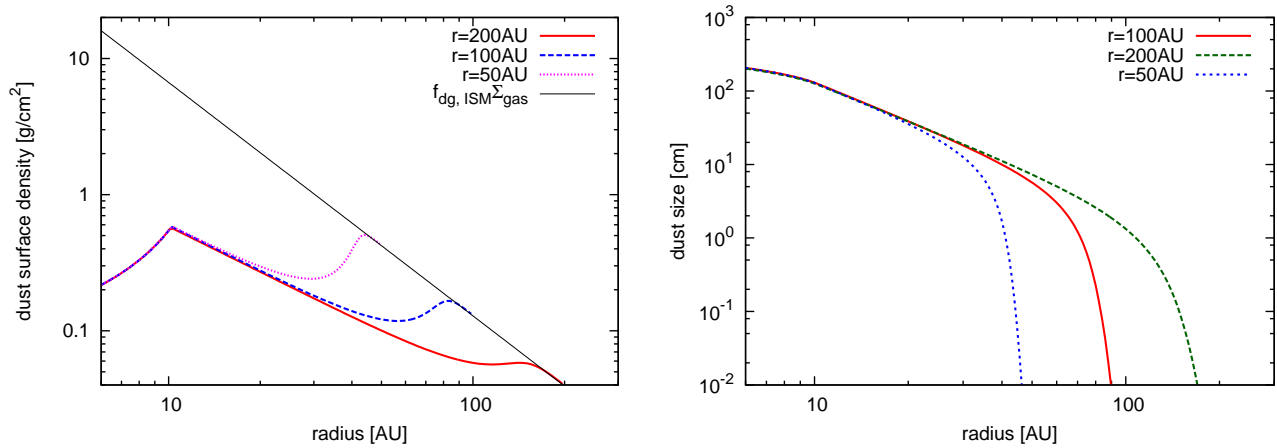


FIG. 10.— Radial profile of dust surface density and dust size in steady state (at $t = 0.2$ Myr) for various disk radii. The red solid, blue dashed, and magenta dotted lines show the profiles of M1Mdot37r200f1, M1Mdot37r100f1, and M1Mdot37r50f1, respectively. The black solid line in the surface density profile shows $f_{\text{dg,ISM}} \Sigma_{\text{gas}}$.

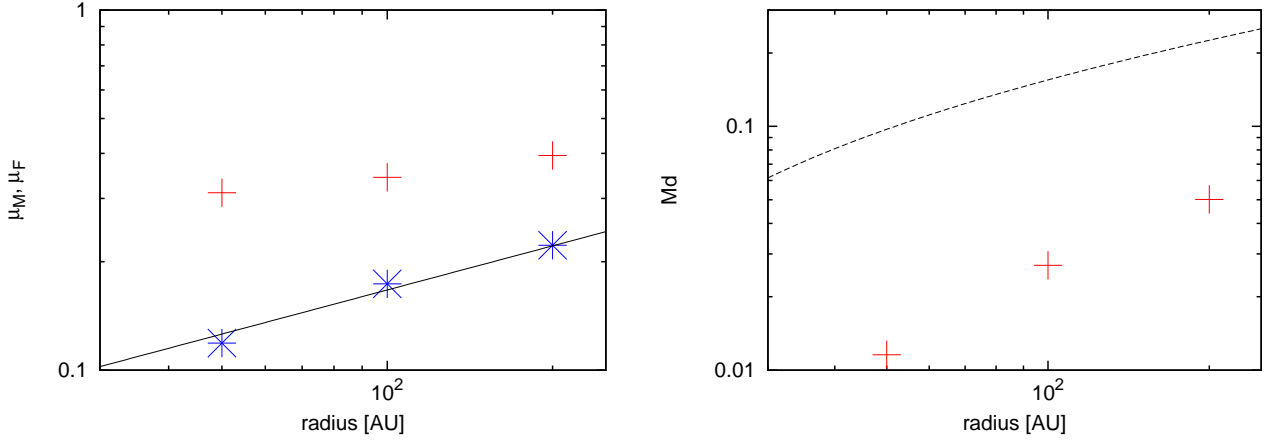


FIG. 11.— Left panel shows the ratio of the dust mass in the steady-state disk (at $t = 0.2$ Myr) to that in the disk with the ISM dust-to-gas mass ratio μ_M , and ratio of the radiative flux from the steady-state disk to that from the disk with the ISM dust-to-gas mass ratio and micron-sized dust μ_F for various disk radii r_{disk} . The red crosses and blue asterisks show μ_M and μ_F , respectively, of M1Mdot37r200f1, M1Mdot37r100f1, and M1Mdot37r50f1. The black solid line shows the empirical formula for μ_F , equation (37). The right panel shows the apparent mass M_{app} of the gas disk. The red crosses show M_{app} . The black dashed line shows the actual mass of the gas disk in our simulation, which asymptotically obeys $M_{\text{gas}} \propto r_{\text{disk}}^{2/7}$.

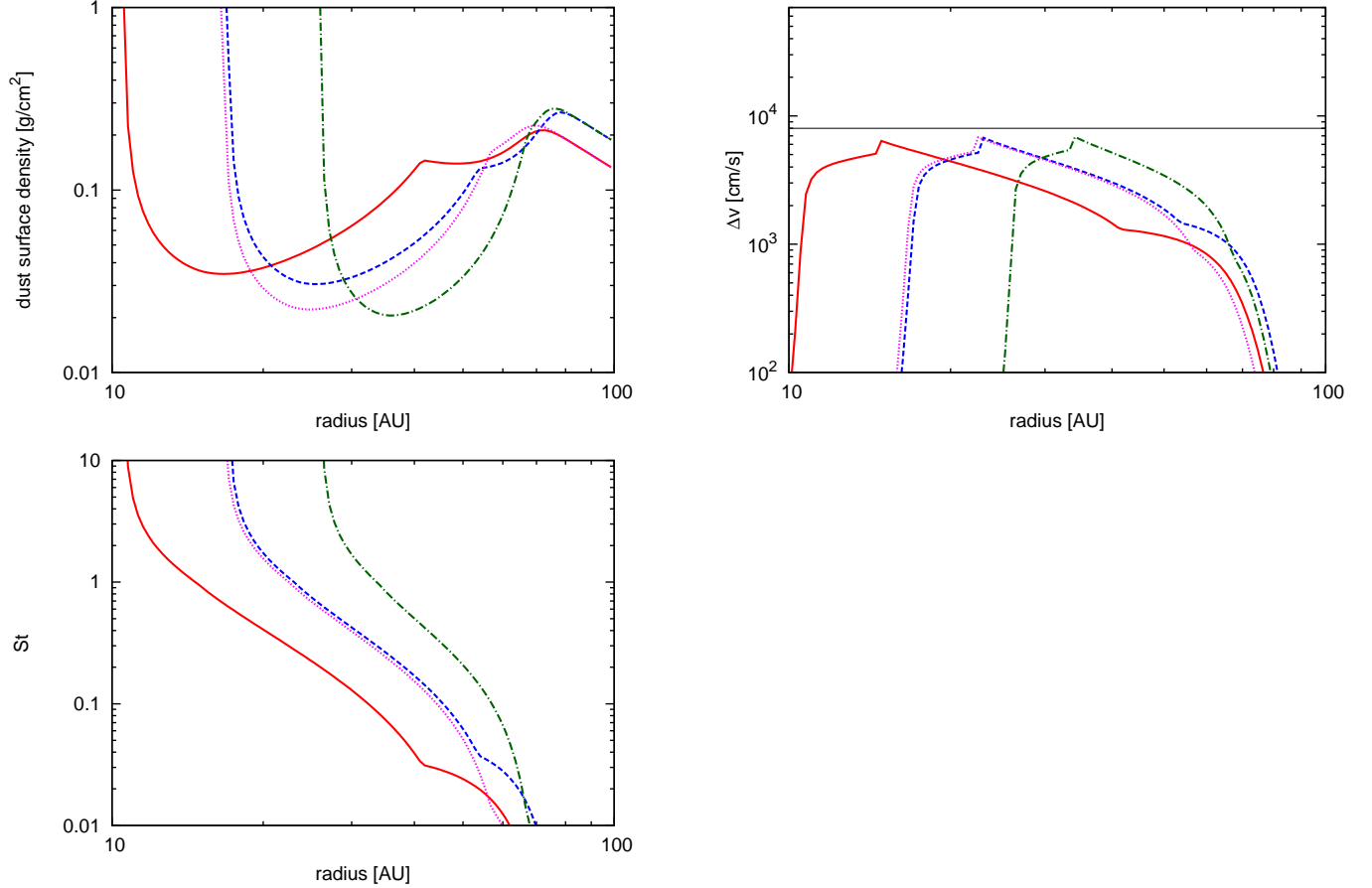


FIG. 12.— Radial profiles of dust surface density, Stokes number, and collision velocity in the steady state for models in which planetesimals form at $r > 10$ AU. The red solid, blue dashed, and magenta dotted, green dashed-dotted lines show the profiles of M1Mdot37r100f4, M2Mdot37r100f4, M1Mdot37r100f5, and M2Mdot37r100f5, respectively. In all models shown in this figure, equation (17) is employed. The black solid line in the right panel shows the threshold velocity.

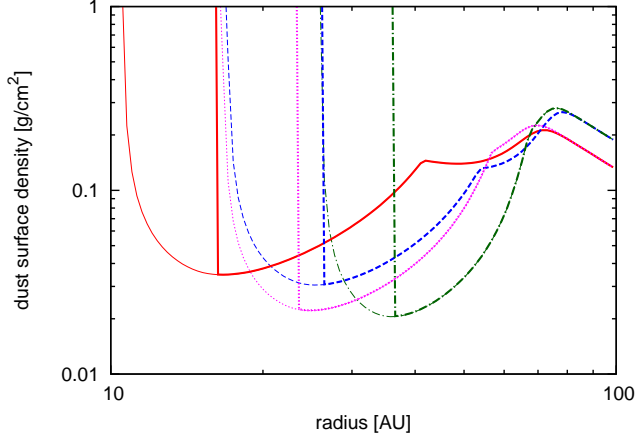


FIG. 13.— Radial profiles of dust surface density in the steady state (at $t = 0.2$ Myr) of the The red solid, blue dashed, and magenta dotted, green dashed-dotted lines show the profiles of M1Mdot37r100f4, M2Mdot37r100f4, M1Mdot37r100f5, and M2Mdot37r100f5, respectively. In all models shown with thick lines, equation (15) is employed, while equation (17) is employed in the models shown with thin lines; these models are identical to that in figure (12).

4.1. Summary

Our findings are summarized as follows.

1. The dust disk quickly settles into the steady state and the total dust mass in the steady state of gravitationally unstable disks in Class 0/I YSOs systematically decreases from that of a disk with ISM dust-to-gas mass ratio. The reduction rate μ_M is 1/2 to 1/3 depending on the mass accretion rate, disk radius, and mass of the central star. The internal density of the dust aggregates only has a minimal effect on the reduction rate.
2. The radiative flux of dust thermal emission from a steady state disk also systematically decreases by a factor of 1/3 to 1/5 from that of a disk with ISM dust-to-gas mass ratio and micron-sized dust. This reduction is caused both by dust depletion and a decrease in opacity owing to dust growth. Because ISM dust-to-gas mass ratio (typically 1/100) and micron-sized dust (typically $0.1\mu\text{m}$) are often assumed in the estimate of the gas disk mass from dust thermal emissions, our results suggest that the gas mass of gravitationally unstable disk is underestimated by a factor of 1/3 to 1/5.
3. Even when a gravitationally unstable disk exists in Class 0/I YSOs, the typical value of the apparent disk mass estimated from dust thermal emission is $\sim 0.03 M_\odot$ and has a $0.01 M_\odot \lesssim M_{\text{app}} \lesssim 0.1 M_\odot$ range. The apparent disk mass has positive dependence on the mass accretion rate from the envelope and disk radius but is almost independent of the dust internal density and mass of the central star. The apparent disk mass is consistent with the disk mass of Class 0/I YSOs estimated from observation, and this apparent reduction suggests that a larger fraction Class 0/I YSO disks is gravitationally unstable than previously believed.
4. The asymptotic steady-state solutions for dust structures is derived (discussed in Appendix A). The solutions are applicable to arbitrary disks in which the radial drift determines the dust structure. For example, in the gravitationally unstable gas disk considered in this paper, the dust surface density asymptotically obeys the power law of $\Sigma_{\text{dust}} \propto r^{-31/28}$ in the Epstein regime, when $\Delta v = \sqrt{\alpha c_s^2 \text{St}}$ and $H_{\text{dust}} = (\text{St}/\alpha)^{-1/2} H_{\text{gas}}$.
5. In the gravitationally unstable disk, planetesimals can form at $r \sim 20$ AU around a $1 M_\odot$ protostar via the planetesimal formation mechanism suggested by Okuzumi et al. (2012) and Kataoka et al. (2013). Because the gas surface density of the gravitationally unstable disk is the theoretical maximum and the orbital radius of planetesimal formation r_P is an increasing function of the gas surface density, this value is the theoretical maximum. Thus, planetesimal formation at $r \gtrsim 20$ AU for a $1 M_\odot$ protostar by the mechanism is highly unlikely because of the radial drift barrier. Some outer migration mechanisms, such as the outer migration of planets (Malhotra 1995; Levison & Morbidelli

2003; Tsukamoto 2011) would be required to explain the existence of planetesimals for $r \gtrsim 20$ AU in the solar system.

4.2. Discussion

4.2.1. Comparison to observations

Our estimate of the apparent mass of a gravitationally unstable disk is consistent with the disk masses of Class 0/I YSOs estimated from dust thermal emission. Andrews & Williams (2007) observed YSOs in Ophiuchus and showed that the disk mass of Class I YSOs is typically $0.015 M_\odot$ and has a range of $0.01 M_\odot < M_{\text{gas,obs}} < 0.1 M_\odot$. Jørgensen et al. (2009) observed 20 Class 0/I YSOs and showed that the typical disk mass of Class 0/I YSOs is approximately $0.05 M_\odot$. Jørgensen et al. (2009) pointed out that their theoretical model for disk evolution tends to produce a larger mass than the observationally estimated value. We propose that this inconsistency comes from the growth and depletion of the dust aggregate. Enoch et al. (2011) observed Class 0 YSOs and suggested that the typical disk mass is about $0.2 M_\odot$, which is larger than the value suggested in other observational studies. Because the apparent disk mass is an increasing function of mass accretion rate, as shown in figure 4, the large mass obtained in Enoch et al. (2011) can be explained if the mass accretion from the envelope is large. It is also possible that the dust disk has still not converged to the steady-state structure in the Class 0 phase because of its young age. In this case, the difference between M_{gas} and M_{app} becomes small. Note also that contamination of the envelope or temperature variation may also cause overestimation of the disk mass, as was noted by these researchers. Because the masses of Class 0/I YSOs are consistent with or slightly larger than our apparent disk mass, we conclude that a larger fraction of the Class 0/I disks than previously considered are gravitationally unstable.

One may think that the decrease of dust-to-gas mass ratio suggested in this paper is inconsistent with the recent observational study that reports large dust-to-gas mass ratio $\sim 1/10$ of evolved disks in Lupus (Ansdell et al. 2016). Note, however, that the gas mass is estimated from the CO line emissions and, as authors noted, whether the large dust-to-gas mass ratio indicates rapid gas loss or depletion of CO by the chemical evolution is unclear (see also Miotello et al. (2016)). Note also that the age of the objects are 1 – 3 Myr and they are not in Class 0/I phase. Therefore, these observations do not directly contradict our results because of uncertainty of chemical evolution and different evolutionary stages.

One may also think that the disk-mass independence of the central-star mass suggested in this paper contradicts observational results of positive correlation between stellar mass and disk mass (Williams & Cieza 2011; Andrews et al. 2013). However, the apparent disk-mass depends on the mass accretion rate and the disk radius, and it is possible that these parameters have correlations to the central-star mass. If this is the case, the disk-mass is indirectly correlated to the central-star mass in Class 0/I YSOs. Note also that the positive correlation were reported based on the observations of Class II YSOs and the results cannot be directly applied to Class 0/I YSOs.

4.2.2. Empirical formula of dust-to-gas mass ratio for a gravitationally unstable disk in Class 0/I YSOs

Because μ_F is the apparent reduction rate of the gas disk mass and is useful for comparing theoretical and observational results, we derive the empirical formula for μ_F using the conjugate gradient method as,

$$\mu_F = 0.17 \left(\frac{\dot{M}_{\text{gas}}}{3 \times 10^{-7} M_{\odot} \text{ yr}^{-1}} \right)^{0.17} \left(\frac{M_{\text{star}}}{1 M_{\odot}} \right)^{-0.53} \left(\frac{f}{10^{-1}} \right)^{0.0048} \left(\frac{r_{\text{disk}}}{100 \text{ AU}} \right)^{0.41}. \quad (37)$$

To derive this formula, we examined the steady-state structures of 144 simulations in total with different parameter sets. We examined the following parameters: $\dot{M}_{\text{gas}} = \{1 \times 10^{-7}, 3 \times 10^{-7}, 1 \times 10^{-6}, 3 \times 10^{-6}\} M_{\odot} \text{ yr}^{-1}$, $M_{\text{star}} = \{0.5, 1.0, 2.0\} M_{\odot}$, $f = \{10^{-4}, 10^{-3}, 10^{-2}, 10^{-1}\}$, and $r = \{50, 100, 200\} \text{ AU}$. We omitted the datasets with $f = 1$ because they may be unlikely to occur in realistic situations and the sudden jump at $f = 1$ (see figure 9) results in an incorrect fit for $f \leq 10^{-1}$. Therefore, we cannot use the empirical formula for $f > 10^{-1}$.

Because μ_F indicates the extent to which the disk mass is underestimated from that with the ISM dust-to-gas mass ratio and the micron-sized dust, we can calculate the "effective" dust-to-gas mass ratio $f_{\text{dg,eff}}$ for a gravitationally unstable disk as

$$f_{\text{dg,eff}} \equiv \mu_F f_{\text{dg,ISM}} = 1.7 \times 10^{-3} \left(\frac{\dot{M}_{\text{gas}}}{3 \times 10^{-7} M_{\odot} \text{ yr}^{-1}} \right)^{0.17} \left(\frac{M_{\text{star}}}{1 M_{\odot}} \right)^{-0.53} \left(\frac{f}{10^{-1}} \right)^{0.0048} \left(\frac{r_{\text{disk}}}{100 \text{ AU}} \right)^{0.41} \left(\frac{f_{\text{dg,ISM}}}{10^{-2}} \right), \quad (38)$$

where $f_{\text{dg,ISM}}$ is the dust-to-gas mass ratio of the ISM.

We can test whether observed Class 0/I YSO disk is gravitationally unstable using equation (38) and the following procedure. First, we calculate the trial gas disk mass using

$$M_{\text{trial}} \equiv f_{\text{dg,eff}}^{-1} M_{\text{dust}}, \quad (39)$$

where M_{dust} is the dust mass derived from the dust thermal emission under the assumption of standard micron-sized dust opacity. Then, we derive the mass of the gravitationally unstable disk as

$$M_{\text{GI}} = \int 2\pi r \Sigma_{\text{GI}}(r) dr \sim 8.6 \times 10^{-2} \left(\frac{M_{\text{star}}}{1 M_{\odot}} \right)^{1/2} \left(\frac{Q_{\text{crit}}}{2} \right)^{-1} (r_{\text{out}}^{2/7} - r_{\text{in}}^{2/7}) M_{\odot}, \quad (40)$$

Here, r_{in} and r_{out} are the inner and outer radii of the disk in astronomical units, respectively. Q_{crit} is the critical Q value, with the $1 \lesssim Q_{\text{crit}} \lesssim 2$. The temperature is assumed to be given by equation (7). If M_{trial} is comparable to M_{GI} , we can conclude that the disk is gravitationally unstable. On the other hand, when $M_{\text{trial}} < M_{\text{GI}}$, the disk is gravitationally stable.

4.2.3. Appearance of gravitationally unstable disk: Do spiral arms always exist?

Although a gravitationally unstable disk is often considered to have spiral arms, this is not always true. GI has an episodic nature and spiral arms emerge only when GI is triggered. The viscous α could temporally increase to a value as large as $\alpha_{\text{temp}} \sim 1$ when the spiral arms are fully developed. Once the surface density is redistributed by GI, α_{temp} decays to a small value until the disk once again becomes sufficiently massive for gravitational instability to develop. This episodic nature is neglected in the steady accretion disk model using time-averaged value of α . When we consider a gravitationally unstable steady disk with $\alpha \sim 0.1$, this means that the spiral arms appear only for a duration of $\sim (\alpha/\alpha_{\text{temp}}) t_{\text{lifetime}} \sim 0.05 \text{ Myr}$ during the entire life time of a Class 0/I YSO where $t_{\text{lifetime}} \sim 0.5 \text{ Myr}$ is the life time of a Class 0/I YSO. Therefore, we expect that we have less chance to observe spiral arms in the Class 0/I phase, even though the disk is marginally gravitationally unstable.

Note, however, that recent observations have found that some YSOs have spiral structures possibly explainable by GI. The grand designed spiral structures are found in Elias 2-27, which is classified as Class II YSO (Pérez et al. 2016). Although Pérez et al. (2016) suggested that the structures are spiral density waves, they can also be explained by gravitational instability as suggested by Tomida et al. (2017). Tobin et al. (2016) found that the triple protostar system L1448 IRS 3B, which is classified as a Class 0 YSO, has the spiral structures. A compact multiple stellar system with spiral arms would be explained by fragmentation of the gravitationally unstable disk (Stamatellos & Whitworth 2009; Vorobyov & Basu 2010a; Nayakshin 2010; Tsukamoto et al. 2015c; Takahashi et al. 2016; Mercer & Stamatellos 2017). Although the degree of ubiquity of spiral structures is still unclear, these observations suggest the importance of investigating gravitationally unstable disks in Class 0/I YSOs in greater detail.

4.2.4. Planetesimal formation in Class 0/I YSOs

We suggest that Class 0/I YSOs are better sites for planetesimal formation than Class II YSOs, which are commonly thought to be the formation sites of planetesimals and planets. One of the most important advantage for considering planetesimal formation in the Class 0/I phase is that a large amount of solid material is available in this phase. Because dust particles inevitably grow and radially migrate in a short timescale (see equation (22)), the total amount of dust that passes thorough the disk is an important quantity for planetesimal formation. Owing to envelope-to-disk accretion, a significant amount of dust (approximately $10^{-2} M_{\odot}$ during the formation of a $1 M_{\odot}$ protostar) is supplied to the disk during the Class 0/I phase. Therefore, the efficiency of planetesimal formation required to produce planetesimals for a solar system-like planetary system in which the mass of solid material is about $10^{-4} M_{\odot}$ is only $\sim 1 \%$. Thus, an inefficient planetesimal formation process is adequate. On the other hand, the dust mass in Class II YSOs is typically $M_{\text{dust}} \lesssim 10^{-4} M_{\odot}$ and there is no dust supply by envelope-to-disk mass accretion. Thus, the total amount

of the dust passing through the disk is approximately two orders of magnitude smaller than that in the Class 0/I phase and is comparable to that in the solar system. Therefore, almost 100 % efficiency for planetesimal and subsequent planet formation is necessary to produce a solar system-like planetary system if planetesimal formation starts in the Class II phase.

Furthermore, it is also expected that the gas surface density in Class II phase is smaller than that in the Class 0/I phase, which makes planetesimals formation at larger orbital radius difficult. As shown in this paper, planetesimals can form at $r \sim 20$ AU in a the gravitationally unstable disk. On the other hand, in a disk with smaller gas surface density, overcoming the radial drift barrier becomes more difficult because the mean free path increases as Σ_{gas} decreases and the dust aggregate enters the Stokes regime at a smaller radius. As shown in Okuzumi et al. (2012), planetesimals can only form within 10 AU in the disk of minimum mass solar nebula model. For these two reasons, we suggest that Class 0/I YSOs are preferable site for planetesimal formation.

Once planetesimals form, they are decoupled from the gas, and radial migration is negligible until they grow to planets at which point Type I migration becomes important. Therefore, solid material can be stored in the form of planetesimals in the disks of Class 0/I YSOs. Note that storing solid material in the form of small dust particles is highly difficult because of its short growth timescale and rapid radial migration (Dullemond & Dominik 2005; Brauer et al. 2007; Birnstiel et al. 2009).

4.2.5. Influence of outburst events

Although there are several advantages for planetesimal formation in Class 0/I YSOs, powerful outburst phenomena expected in the Class 0/I phase can possibly have negative impact on planetesimal formation by extending the snow line toward several tens of AU and reprocessing the icy dust particles. Here, we focus on the FU Ori outbursts because other outburst phenomena, such as EX Lup outbursts, are relatively weak (see for example Hillenbrand & Findeisen 2015) and negligible.

During FU Ori outbursts, the brightness increases by 4-6 magnitude on the timescale of months to years and gradually decays over a timescales of 100 years (Herbig 1989). Once the stellar luminosity increases to several $100 L_{\odot}$, the H_2O snow line moves to several tens of AU. Recent observation of the FU Ori type star V883 Ori actually detected the H_2O snow line at ~ 40 AU (Cieza et al. 2016). Inside the snow line, H_2O is vaporized within a short time. When an outburst ceases, the vaporized H_2O will condense onto the dust particles. Through this evaporation and condensation process, the properties of the dust particles change; in particular, dust porosity would increase (dust particles are compacted), which means that the outburst has a negative impact on planetesimal formation via coagulation of porous dust aggregates.

Here, we roughly estimate the distance of snow line as a function of the luminosity. By assuming the H_2O vaporization happens at $T_{\text{vapor}} = 170$ K and disk temperature depends on the stellar luminosity as $T \propto L^{3/7}$ (Garaud & Lin 2007), the distance of the snow line from

the central star is calculated by solving $T_{\text{disk}} = 150 \times (L/L_{\odot})^{3/7} (r/1\text{AU})^{-3/7} = T_{\text{vapor}}$,

$$r_{\text{snow}} \sim 41 \left(\frac{L}{400L_{\odot}} \right)^{2/3} \text{ AU}. \quad (41)$$

This estimate is consistent with the snow line found in V883 Ori, whose bolometric luminosity is estimated as $400L_{\odot}$.

Whether burst events have a large impact on planetesimal formation in the Class 0/I phase critically depends on the intervals between outburst events and on their magnitude. Dust particles processed by an outburst drift toward the central star and disappear, while unprocessed fresh dust particles are refilled, on the radial drift timescale. Therefore, if the radial drift timescale or the refilling timescale is smaller than the outburst interval, most of the dust does not undergo outburst processing.

Using equation (A14) and (41), the radial drift (refilling) timescale in the Epstein regime is estimated as

$$t_{\text{drift, Epstein}} = \frac{r}{v_{r, \text{dust}}} \sim 2.6 \times 10^4 \left(\frac{L}{400L_{\odot}} \right)^{25/42} \left(\frac{\dot{M}}{10^{-6} M_{\odot} \text{ yr}^{-1}} \right)^{-1/2} \text{ years}, \quad (42)$$

as a function of the stellar luminosity.

This is an upper limit on the drift timescale because the porous dust enters the Stokes regime at several tens of AU and $v_{r, \text{dust}}$ becomes much larger than the value of equation (A14). Using equation (A17) and (41), and assuming $\Delta v = \sqrt{\alpha c_s^2 \text{St}}$ and $H_{\text{dust}} = (\text{St}/\alpha)^{-1/2} H_{\text{gas}}$, the radial drift timescale in the Stokes regime is estimated as

$$t_{\text{drift, Stokes}} \sim 2.7 \times 10^3 \left(\frac{L}{400L_{\odot}} \right)^{103/63} \left(\frac{\dot{M}}{10^{-6} M_{\odot} \text{ yr}^{-1}} \right)^{-2/3} \left(\frac{M}{1 M_{\odot}} \right)^{-2/3} \left(\frac{\rho_{\text{int}}}{10^{-4}} \right)^{1/3} \text{ years}. \quad (43)$$

This is a lower limit on the drift timescale because the dust radial profile does not quickly converge to this asymptotic solution and the assumption of $\text{St} \ll 1$ is no longer valid at the inner region of the disk. In the realistic situation, it is expected that the refilling timescale is between $t_{\text{drift, Stokes}}$ and $t_{\text{drift, Epstein}}$. These can be regarded as the timescales for which the system forgets an outburst with luminosity L . If an outburst with a maximum luminosity of L repeatedly occurs with an interval smaller than t_{drift} years, it alters the planetesimal formation process suggested in this paper.

Although the event rate of outbursts is highly uncertain, it is estimated as 10^{-4} to 10^{-5} per year per protostar (Hartmann & Kenyon 1996; Hillenbrand & Findeisen 2015; Hartmann et al. 2016), suggesting a interval timescale $t_{\text{interval}} \sim 10^4 - 10^5$ years. t_{interval} seems to be comparable or slightly larger than t_{drift} . Furthermore, t_{interval} is estimated using all FU Ori outbursts, but some of them are not strong enough to extend the snow line to several tens of AU. The bolometric luminosity of FU Ori objects ranges

$20 < L_{\text{bol}} < 550L_{\odot}$ (Sandell & Weintraub 2001) and a stellar luminosity of $L \sim 400L_{\odot}$ seems to be closer to the maximum of the FU Ori outbursts. Thus, it is expected that the event rate of strong outbursts that move the snow line to several tens of AU is smaller than the estimate of 10^{-4} to 10^{-5} per year per protostar.

Because the t_{drift} is $\sim 10^4$ years and is expected to be smaller for porous dust aggregates, and the interval timescale of the strong outburst is expected to be larger than 10^4 years, we conclude that the influence of outburst events is limited and that planetesimal formation in Class 0/I YSOs is still a promising pathway to producing planetesimals at the outer radius (> 10 AU), although strong outburst events may decrease the efficiency of planetesimal formation in the Class 0/I phase.

On the other hand, outbursts may have little influence on apparent disk mass reduction. As shown in equation (37), the reduction rate weakly depends on the dust porosity. Furthermore, the outer region of the disk tends to have a larger contribution to the thermal radiation. Thus, changes in the dust properties within several tens of AU would not significantly affect the apparent disk-mass estimated from dust thermal emission.

4.2.6. Importance of considering planet formation in Class 0/I YSOs

Because planetesimals can form even in the Class 0/I phase, investigating the planet formation process in this phase is an interesting subject. As discussed above, there are several advantages for planetesimal formation in the Class 0/I phase. In particular, planetesimal formation at $r > 10$ AU requires a large surface density corresponding to $Q \sim 1$. There is also an advantage associated with considering planet formation in the Class 0/I phase. As shown in figure 3, dust aggregates pass through the disk in the form of "pebbles". Previous studies have shown that planetary seeds can grow quickly with pebble accretion (Ormel & Klahr 2010; Lambrechts & Johansen 2012, 2014; Ida et al. 2016). In the Class 0/I phase, dust particles are supplied via envelope accretion with a high mass accretion rate of $\dot{M}_{\text{dust}} \sim f_{\text{dg,ISM}} \dot{M}_{\text{gas}} \sim 10^{-8} - 10^{-9} M_{\odot} \text{ yr}^{-1}$. This period has a duration of ~ 0.5 Myr. Under such a large accretion rate, proto-planet formation is accelerated significantly, especially at $r > 10$ AU (Ida et al. 2016). On the other hand, in the Class II phase, pebble accretion may stop within a short

duration because of the depletion of dust at the outer edge of the disk. As shown in Lambrechts & Johansen (2014), even starting from a disk with the ISM dust-to-gas mass ratio and micron-sized dust particles, dust particles in a disk of 100 AU in size deplete at ~ 1 Myr (this roughly corresponds to the dust growth timescale at the outer edge). As pointed out by Ida et al. (2016), depletion of dust at the outer disk edge is a serious problem for the pebble accretion scenario in an isolated disk. Furthermore, at the beginning of the Class II phase, the dust-to-gas mass ratio may already be much smaller than $f_{\text{dg,ISM}}$ and the dust particles have already grown to centimeter-size, even around the edge, as shown in our simulations. Therefore, dust depletion occurs over a shorter period of time than that previously considered in the Class II phase. Thus, planet formation via the pebble accretion scenario may be preferred in Class 0/I YSOs.

Recent observations of HL Tau, which is classified as being in the late Class I phase, found the multiple ring structures in the dust disk (ALMA Partnership et al. 2015) and possibly in the gas disk (Yen et al. 2016). To explain the ring structures, several mechanisms, such as dust growth near the condensation front of volatiles (Zhang et al. 2015, 2016), sintering-induced ring formation (Okuzumi et al. 2016), secular gravitational instability (Takahashi & Inutsuka 2014, 2016), or gap opening by planets (Dipierro et al. 2015; Kanagawa et al. 2015, 2016), have been proposed.

If the gaps are induced by planets, an obvious question is how these planets form in the very early phase of star formation (the age of HL Tau is $\lesssim 1$ Myr). In this paper, we proposed the possibility of planetesimal formation in Class 0/I YSOs. However, whether planetesimals can grow into the planets within the Class I phase is an open question. The discovery of multiple rings also suggests the importance of investigating the possibility of planet formation in the Class 0/I phase.

ACKNOWLEDGMENTS

We thank Dr. H. Tanaka, Dr. H. Kobayashi, Dr. S. Takahashi, Dr. S. Inutsuka, Dr. Y. Imaeda, Dr. M. Kunimoto, Dr. T. Muto, for their fruitful discussions. We also thank the anonymous referee for his/her insightful comments.

APPENDIX

A: ANALYTIC SOLUTIONS FOR STEADY-STATE STRUCTURE OF DUST DISK

In this appendix, we derive the asymptotic steady-state solution for a dust disk in which dust radial drift dominates. Although, we focus on the dust structure of a gravitationally unstable disk, the solution is applicable to an arbitrary gas disk structure.

governing equations

Through omission of the time derivatives of equations (13) and (14), the governing equations for the steady-state solutions are given as

$$\frac{1}{r} \frac{\partial}{\partial r} (r v_{r,\text{dust}} \Sigma_{\text{dust}}) = 0, \quad (\text{A1})$$

$$v_{r,\text{dust}} \frac{\partial m_{\text{dust}}}{\partial r} = \frac{m_{\text{dust}}}{t_{\text{coll}}}. \quad (\text{A2})$$

Equation (A1) is easily integrated and the mass conservation of dust in the steady state is expressed as

$$2\pi r |v_{r,\text{dust}}| \Sigma_{\text{dust}} = \dot{M}_{\text{dust}} (= \text{const}). \quad (\text{A3})$$

On the other hand, equation (A2) can be rewritten as

$$\frac{\partial a_{\text{dust}}(r)}{\partial r} = - \left(\frac{1}{2\pi} \right)^{3/2} \left(\frac{m_{\text{gas}}^2 v_{\text{K}}^2 \dot{M}_{\text{dust}}}{r k_B^2 T^2 (d \ln P / d \ln r)^2 \rho_{\text{int}}} \right) \left(\frac{\Delta v}{H_{\text{dust}} \text{St}^2} \right) \quad (\text{A4})$$

where we use equation (A3), $m_{\text{dust}} = (4\pi/3)\rho_{\text{int}}a_{\text{dust}}^3$, $n_{\text{dust}} = \Sigma_{\text{dust}}/(\sqrt{2\pi}H_{\text{dust}}m_{\text{dust}})$, $v_{r,\text{dust}} = -2\eta v_{\text{K}}\text{St}$, and assumed that $\text{St} \ll 1$.

Note that the variables in the second bracket are constant or depend only on the gas disk structure; on the other hand, those in the third bracket depend on a_{dust} . Thus, we can solve equation (A4) by specifying the relative velocity, dust scale height, and drag law.

Steady-state solutions for dust disk

First, we derive the steady-state solution for the case in which the drag law is given by the Epstein drag law and the relative velocity and dust scale height are given as $\Delta v = \sqrt{\alpha c_s^2 \text{St}}$ and $H_{\text{dust}} = (\text{St}/\alpha)^{-1/2} H_g$, respectively. In this case, equation (A4) becomes

$$\frac{\partial a_{\text{dust}}(r)}{\partial r} = - \left(\frac{\dot{M}_{\text{dust}} m_{\text{gas}}^2 v_{\text{K}}^3 \Sigma_{\text{gas}}}{(2\pi^5)^{1/2} k_B^2 T^2 (d \ln P / d \ln r)^2 \rho_{\text{int}}^2} \right) r^{-2} a_{\text{dust}}(r)^{-1}. \quad (\text{A5})$$

By assuming that the gas disk profile can be expressed as the power law $\Sigma_{\text{gas}}(r) = \Sigma_0 r^{-n_\Sigma}$, $T(r) = T_0 r^{-n_T}$, $\alpha(r) = \alpha_0 r^{n_\alpha}$, $v_{\text{K}}(r) = v_{\text{K},0} r^{-n_K}$, we can rewrite equation (A5) as

$$\begin{aligned} \frac{\partial a_{\text{dust}}(r)}{\partial r} &= - \left(\frac{\dot{M}_{\text{dust}} m_{\text{gas}}^2 v_{\text{K},0}^3 \Sigma_0}{(2\pi^5)^{1/2} (d \ln P / d \ln r)^2 k_B^2 T_0^2 \rho_{\text{int}}^2} \right) \times \\ &\quad r^{-2+2n_T-3n_K-n_\Sigma} a_{\text{dust}}(r)^{-1} \\ &\equiv A r^{-2+2n_T-3n_K-n_\Sigma} a_{\text{dust}}(r)^{-1}, \end{aligned} \quad (\text{A6})$$

where A is a negative constant. Solution of (A6) is given as

$$a_{\text{dust}}(r) = \left(\frac{2A}{-1+2n_T-3n_K-n_\Sigma} r^{-1+2n_T-3n_K-n_\Sigma} + C \right)^{\frac{1}{2}}, \quad (\text{A7})$$

where C is a constant. Because the power law index of r , $(-1+2n_T-3n_K-n_\Sigma)$ is negative for the gas disk used in this paper, $((-1+2n_T-3n_K-n_\Sigma) = -47/14 < 0)$, the dust size asymptotically converges to the power law

$$a_{\text{dust}}(r) \rightarrow \left(\frac{2A}{-1+2n_T-3n_K-n_\Sigma} r^{-1+2n_T-3n_K-n_\Sigma} \right)^{\frac{1}{2}} \quad (r \rightarrow 0) \quad (\text{A8})$$

Using this asymptotic solution, we can show that the ratio of the collision timescale t_{coll} and the drift timescale $t_{\text{drift}} \equiv r/v_{r,\text{dust}}$ converges to a constant value as

$$\mu_{\text{dust}} \equiv \frac{t_{\text{coll}}}{t_{\text{drift}}} \rightarrow \frac{2}{3(1-2n_T+3n_K+n_\Sigma)} \quad (r \rightarrow 0). \quad (\text{A9})$$

The asymptotic value of μ_{dust} is determined by the power indices of the gas disk. For the gas disk model used in this paper,

$$\mu_{\text{dust}} = \frac{2}{3(1-2n_T+3n_K+n_\Sigma)} = \frac{28}{141}, \quad (\text{A10})$$

where we use equations (8) – (9) and $v_{\text{K}} \propto r^{-1/2}$. The fact that $\mu_{\text{dust}} \rightarrow \text{const}$ ($r \rightarrow 0$) has already been pointed out by Okuzumi et al. (2016). The new finding in this section is that the value of μ_{dust} depends on the gas disk structure and there is no universal value for μ_{dust} .

Once the asymptotic solution for dust size (or equivalently, the value of $t_{\text{coll}}/t_{\text{drift}}$) is determined, the dust surface density, Stokes number, collision velocity, and radial drift velocity are determined by equation (A3), $\text{St} = (\pi \rho_{\text{int}} a_{\text{dust}}) / (2 \Sigma_{\text{gas}})$, $\Delta v = \sqrt{\alpha c_s^2 \text{St}}$, and $v_{r,\text{dust}} = -2\eta v_{\text{K}} \text{St}$, respectively. The asymptotic steady-state solution of

the dust structure for our gas disk model (equations (7), (8), and (9)) can be calculated as

$$\Sigma_{\text{dust}} = 1.0 \left(\frac{r}{10 \text{ AU}} \right)^{-\frac{31}{28}} \left(\frac{\dot{M}_{\text{gas}}}{10^{-6} M_{\odot} \text{ yr}^{-1}} \right)^{\frac{1}{2}} \text{ g cm}^{-2} \quad (\text{A11})$$

$$\text{St} = 9.0 \times 10^{-2} \left(\frac{r}{10 \text{ AU}} \right)^{\frac{1}{28}} \left(\frac{\dot{M}_{\text{gas}}}{10^{-6} M_{\odot} \text{ yr}^{-1}} \right)^{\frac{1}{2}} \left(\frac{M_{\text{star}}}{1 M_{\odot}} \right)^{\frac{1}{2}} \quad (\text{A12})$$

$$a_{\text{dust}} = 3.8 \times 10^2 \left(\frac{r}{10 \text{ AU}} \right)^{-\frac{47}{28}} \left(\frac{\dot{M}_{\text{gas}}}{10^{-6} M_{\odot} \text{ yr}^{-1}} \right)^{\frac{1}{2}} \left(\frac{M_{\text{star}}}{1 M_{\odot}} \right) \left(\frac{\rho_{\text{int}}}{0.1 \text{ g cm}^{-3}} \right)^{-1} \text{ cm} \quad (\text{A13})$$

$$v_{\text{r,dust}} = -6.5 \times 10^2 \left(\frac{r}{10 \text{ AU}} \right)^{\frac{3}{28}} \left(\frac{\dot{M}_{\text{gas}}}{10^{-6} M_{\odot} \text{ yr}^{-1}} \right)^{\frac{1}{2}} \text{ cm s}^{-1} \quad (\text{A14})$$

$$\Delta v = 2.8 \times 10^3 \left(\frac{r}{10 \text{ AU}} \right)^{\frac{1}{8}} \left(\frac{\dot{M}_{\text{gas}}}{10^{-6} M_{\odot} \text{ yr}^{-1}} \right)^{\frac{3}{4}} \left(\frac{M_{\text{star}}}{1 M_{\odot}} \right)^{\frac{1}{4}} \text{ cm s}^{-1} \quad (\text{A15})$$

where we assume that the mass accretion rate of the dust is given as $\dot{M}_{\text{dust}} = f_{\text{dg,ISM}} \dot{M}_{\text{gas}}$. We also assume that $\Delta v = \sqrt{2\alpha c_s^2 \text{St}}$ instead of $\Delta v = \sqrt{\alpha c_s^2 \text{St}}$ for consistency with the numerical simulations conducted in this study. The value of μ_{dust} is not affected by the factor of difference of Δv . As already shown in figure 2, this asymptotic solution describes the numerical results well.

The asymptotic value for μ_{dust} in equation (A9) is obtained by assuming $\Delta v = \sqrt{\alpha c_s^2 \text{St}}$, $H_{\text{dust}} = (\text{St}/\alpha)^{-1/2} H_{\text{gas}}$ and the Epstein drag law; however, there are other possibilities. For example, it is possible that the radial drift determines the collision velocity as $\Delta v = \eta v_K \text{St}$, or that the dust scale height is equal to the gas scale height as $H_{\text{dust}} = H_{\text{gas}}$, or that the gas drag is determined by the Stokes drag law. As expected from the term in the third bracket of equation (A6), the asymptotic value of μ_{dust} depends on the forms of Δv , H_{dust} and the drag law. Following the same procedure as that described above, we can calculate the asymptotic value for μ_{dust} with these different assumptions. The asymptotic values for μ_{dust} in the Epstein regime are given as

$$\mu_{\text{dust}} = \begin{cases} \frac{2}{3(1-2n_T+3n_{v_K}+n_{\Sigma})} (\Delta v = \sqrt{\alpha c_s^2 \text{St}} \text{ and } H_{\text{dust}} = (\text{St}/\alpha)^{-1/2} H_{\text{gas}}) \\ \frac{1}{2-3n_T+4n_{v_K}+n_{\alpha}+n_{\Sigma}} (\Delta v = \eta v_K \text{St} \text{ and } H_{\text{dust}} = (\text{St}/\alpha)^{-1/2} H_{\text{gas}}) \\ \frac{5}{3(2-4n_T+6n_{v_K}-n_{\alpha}+3n_{\Sigma})} (\Delta v = \sqrt{\alpha c_s^2 \text{St}} \text{ and } H_{\text{dust}} = H_{\text{gas}}) \end{cases} \quad (\text{A16})$$

In the case of the Stokes regime,

$$\mu_{\text{dust}} = \begin{cases} \frac{2}{-3n_T+4n_{v_K}} (\Delta v = \sqrt{\alpha c_s^2 \text{St}} \text{ and } H_{\text{dust}} = (\text{St}/\alpha)^{-1/2} H_{\text{gas}}) \\ \frac{8}{3(2-5n_T+6n_{v_K}+2n_{\alpha})} (\Delta v = \eta v_K \text{St} \text{ and } H_{\text{dust}} = (\text{St}/\alpha)^{-1/2} H_{\text{gas}}) \\ \frac{16}{3(-2-5n_T+6n_{v_K}-2n_{\alpha})} (\Delta v = \sqrt{\alpha c_s^2 \text{St}} \text{ and } H_{\text{dust}} = H_{\text{gas}}). \end{cases} \quad (\text{A17})$$

When μ_{dust} becomes negative, the asymptotic solutions become complex and physical solutions under the given disk structures and conditions do not exist.

Once μ_{dust} is determined, the asymptotic solution for the dust size and the Stokes number are determined using

$$\frac{t_{\text{coll}}}{t_{\text{drift}}} = \frac{3\Delta v \dot{M}_{\text{dust}}}{2(2\pi)^{3/2} H_{\text{dust}} \eta^2 \text{St}^2 \rho_{\text{int}} a_{\text{dust}}} = \mu_{\text{dust}}, \quad (\text{A18})$$

and equation (12). Then, we can obtain the dust surface density and the drift velocity by equation (A3) and $v_{\text{r,dust}} = -2\eta v_K \text{St}$, respectively.

B: COMPARISON BETWEEN VISCOUS HEATING AND IRRADIATION HEATING

In this paper, we assumed that the disk temperature is determined by stellar irradiation and viscous heating is negligible in outer region ($r > 10 \text{ AU}$). To confirm that viscous heating is negligible in a gravitationally unstable disk

in outer region, we estimate the temperature profile determined by the viscous heating only. When viscous heating determines the disk temperature, the energy balance between the local viscous heating and the local radiation cooling,

$$\left| \frac{d \ln \Omega}{d \ln R} \right|^2 \alpha \frac{c_s^2}{\Omega} \Sigma \Omega^2 = \frac{32 \sigma T_{\text{visc}}^4}{3(\tau_{\text{half}} + \tau_{\text{half}}^{-1})}. \quad (\text{B1})$$

is realized in the disk, where T_{visc} is the midplane temperature in the viscously heated disk, $\tau_{\text{half}} = (1/2)\kappa\Sigma_{\text{gas}}$ is the vertical optical depth, and κ is the opacity. We assume that the opacity obeys the power law

$$\kappa(T) = \kappa_0 T^2 \text{ cm}^2 \text{ g}^{-1}. \quad (\text{B2})$$

This formula approximates the (gray) dust opacity in a low-temperature region, $T < 100$ K (Bell & Lin 1994). κ_0 is typically $10^{-4} \text{ cm}^2 \text{ g}^{-1}$ if we assume a dust-to-gas mass ratio of 1/100. However, as shown in figure 2, the dust-to-gas mass ratio becomes $\sim 1/1000$ and κ_0 becomes $\sim 10^{-5} \text{ cm}^2 \text{ g}^{-1}$ in the steady state of our fiducial model at $r \sim 10$ AU. By solving equations (3), (4), (6), and (B1) and assuming that the disk is vertically optically thick, we obtain the temperature profile of a disk in which the local heating balances with the local radiative cooling

$$T_{\text{visc,thick}} = 58 \left(\frac{r}{10 \text{ AU}} \right)^{-3} \left(\frac{\kappa_0}{10^{-5} \text{ cm}^2 \text{ g}^{-1}} \right)^{2/3} \left(\frac{M_{\text{star}}}{M_{\odot}} \right) \left(\frac{\dot{M}_{\text{gas}}}{10^{-6} M_{\odot} \text{ yr}^{-1}} \right)^{2/3} \text{ K}. \quad (\text{B3})$$

Thus, $T_{\text{visc,thick}}$ is nearly equal to the irradiated temperature T_{irr} at 10 AU, $T = 55$ K, and decreases more rapidly than T_{irr} as r increases. Thus, $T_{\text{visc,thick}} < T_{\text{irr}}$ in almost the entire region of an optically thick disk. On the other hand, the disk may become vertically optically thin in the outer region. The temperature profile for an optically thin disk is given as

$$T_{\text{visc,thin}} = 16 \left(\frac{r}{100 \text{ AU}} \right)^{-3/13} \left(\frac{\kappa_0}{10^{-5} \text{ cm}^2 \text{ g}^{-1}} \right)^{-2/13} \left(\frac{\dot{M}_{\text{gas}}}{10^{-6} M_{\odot} \text{ yr}^{-1}} \right)^{2/13} \text{ K}. \quad (\text{B4})$$

Although the radial dependence of $T_{\text{visc,thin}}$ is shallower than that of T_{irr} , $T_{\text{visc,thin}}$ is smaller than T_{irr} for $r \lesssim 300$ AU. Therefore, at $r > 10$ AU, T_{visc} is smaller than T_{irr} , in both the optically thick and thin cases and we can adopt an approximation in which the stellar irradiation determines the temperature of the entire disk.

REFERENCES

- A'Hearn, M. F., Belton, M. J. S., Delamere, W. A., Kissel, J., Klaasen, K. P., McFadden, L. A., Meech, K. J., Melosh, H. J., Schultz, P. H., Sunshine, J. M., Thomas, P. C., Veverka, J., Yeomans, D. K., Baca, M. W., Busko, I., Crockett, C. J., Collins, S. M., Desnoyer, M., Eberhardy, C. A., Ernst, C. M., Farnham, T. L., Feaga, L., Groussin, O., Hampton, D., Ipatov, S. I., Li, J.-Y., Lindler, D., Lisse, C. M., Mastrodemos, N., Owen, W. M., Richardson, J. E., Wellnitz, D. D., & White, R. L. 2005, *Science*, 310, 258
- Allen, A., Li, Z.-Y., & Shu, F. H. 2003, *ApJ*, 599, 363
- ALMA Partnership, Brogan, C. L., Pérez, L. M., Hunter, T. R., Dent, W. R. F., Hales, A. S., Hills, R. E., Corder, S., Fomalont, E. B., Vlahakis, C., Asaki, Y., Barkats, D., Hirota, A., Hodge, J. A., Impellizzeri, C. M. V., Kneissl, R., Liuzzo, E., Lucas, R., Marcelino, N., Matsushita, S., Nakanishi, K., Phillips, N., Richards, A. M. S., Toledo, I., Aladro, R., Brogiere, D., Cortes, J. R., Cortes, P. C., Espada, D., Galarza, F., Garcia-Appadoo, D., Guzman-Ramirez, L., Humphreys, E. M., Jung, T., Kamenoi, S., Laing, R. A., Leon, S., Marconi, G., Mignano, A., Nikolic, B., Nyman, L.-A., Radiszcz, M., Remijan, A., Rodón, J. A., Sawada, T., Takahashi, S., Tilanus, R. P. J., Vila Vilaro, B., Watson, L. C., Wiklind, T., Akiyama, E., Chapillon, E., de Gregorio-Monsalvo, I., Di Francesco, J., Gueth, F., Kawamura, A., Lee, C.-F., Nguyen Luong, Q., Mangum, J., Pietu, V., Sanhueza, P., Saigo, K., Takakuwa, S., Ubach, C., van Kempen, T., Wootten, A., Castro-Carrizo, A., Francke, H., Gallardo, J., Garcia, J., Gonzalez, S., Hill, T., Kaminski, T., Kurono, Y., Liu, H.-Y., Lopez, C., Morales, F., Plarre, K., Schieven, G., Testi, L., Videla, L., Villard, E., Andreani, P., Hibbard, J. E., & Tatematsu, K. 2015, *ApJ*, 808, L3
- Andrews, S. M., Rosenfeld, K. A., Kraus, A. L., & Wilner, D. J. 2013, *ApJ*, 771, 129
- Andrews, S. M. & Williams, J. P. 2007, *ApJ*, 671, 1800
- Ansdell, M., Williams, J. P., van der Marel, N., Carpenter, J. M., Guidi, G., Hogerheijde, M., Mathews, G. S., Manara, C. F., Miotello, A., Natta, A., Oliveira, I., Tazzari, M., Testi, L., van Dishoeck, E. F., & van Terwisga, S. E. 2016, *ApJ*, 828, 46

- Aso, Y., Ohashi, N., Saigo, K., Koyamatsu, S., Aikawa, Y., Hayashi, M., Machida, M. N., Saito, M., Takakuwa, S., Tomida, K., Tomisaka, K., & Yen, H.-W. 2015, *ApJ*, 812, 27
- Bai, X.-N. & Stone, J. M. 2011, *ApJ*, 736, 144
- Beckwith, S. V. W. & Sargent, A. I. 1991, *ApJ*, 381, 250
- Bell, K. R. & Lin, D. N. C. 1994, *ApJ*, 427, 987
- Bergin, E. A., Cleeves, L. I., Gorti, U., Zhang, K., Blake, G. A., Green, J. D., Andrews, S. M., Evans, II, N. J., Henning, T., Öberg, K., Pontoppidan, K., Qi, C., Salyk, C., & van Dishoeck, E. F. 2013, *Nature*, 493, 644
- Birnstiel, T., Dullemond, C. P., & Brauer, F. 2009, *A&A*, 503, L5
- , 2010, *A&A*, 513, A79
- Birnstiel, T., Klahr, H., & Ercolano, B. 2012, *A&A*, 539, A148
- Brauer, F., Dullemond, C. P., & Henning, T. 2008, *A&A*, 480, 859
- Brauer, F., Dullemond, C. P., Johansen, A., Henning, T., Klahr, H., & Natta, A. 2007, *A&A*, 469, 1169
- Brinch, C., Crapsi, A., Hogerheijde, M. R., & Jørgensen, J. K. 2007, *A&A*, 461, 1037
- Carrasco-González, C., Henning, T., Chandler, C. J., Linz, H., Pérez, L., Rodríguez, L. F., Galván-Madrid, R., Anglada, G., Birnstiel, T., van Boekel, R., Flock, M., Klahr, H., Macías, E., Menten, K., Osorio, M., Testi, L., Torrelles, J. M., & Zhu, Z. 2016, *ApJ*, 821, L16
- Chiang, E. I. & Goldreich, P. 1997, *ApJ*, 490, 368
- Chou, T.-L., Takakuwa, S., Yen, H.-W., Ohashi, N., & Ho, P. T. P. 2014, *ApJ*, 796, 70
- Cieza, L. A., Casassus, S., Tobin, J., Bos, S. P., Williams, J. P., Perez, S., Zhu, Z., Caceres, C., Canovas, H., Dunham, M. M., Hales, A., Prieto, J. L., Principe, D. A., Schreiber, M. R., Ruiz-Rodríguez, D., & Zurlo, A. 2016, *Nature*, 535, 258
- Dipierro, G., Price, D., Laibe, G., Hirsh, K., Cerioli, A., & Lodato, G. 2015, *MNRAS*, 453, L73
- Dubrule, B., Morfill, G., & Sterzik, M. 1995, *Icarus*, 114, 237
- Dullemond, C. P. & Dominik, C. 2005, *A&A*, 434, 971
- Dunham, M. M., Vorobyov, E. I., & Arce, H. G. 2014, *MNRAS*, 444, 887
- Enoch, M. L., Corder, S., Duchêne, G., Bock, D. C., Bolatto, A. D., Culverhouse, T. L., Kwon, W., Lamb, J. W., Leitch, E. M., Marrone, D. P., Muchovej, S. J., Pérez, L. M., Scott, S. L., Teuben, P. J., Wright, M. C. H., & Zauderer, B. A. 2011, *ApJS*, 195, 21
- Evans, II, N. J., Dunham, M. M., Jørgensen, J. K., Enoch, M. L., Merín, B., van Dishoeck, E. F., Alcalá, J. M., Myers, P. C., Stapelfeldt, K. R., Huard, T. L., Allen, L. E., Harvey, P. M., van Kempen, T., Blake, G. A., Koerner, D. W., Mundy, L. G., Padgett, D. L., & Sargent, A. I. 2009, *ApJS*, 181, 321
- Fleming, T. P., Stone, J. M., & Hawley, J. F. 2000, *ApJ*, 530, 464
- Garaud, P. & Lin, D. N. C. 2007, *ApJ*, 654, 606
- Hartmann, L., Calvet, N., Gullbring, E., & D'Alessio, P. 1998, *ApJ*, 495, 385
- Hartmann, L., Herczeg, G., & Calvet, N. 2016, *ARA&A*, 54, 135
- Hartmann, L. & Kenyon, S. J. 1996, *ARA&A*, 34, 207
- Herbig, G. H. 1989, in *European Southern Observatory Conference and Workshop Proceedings*, Vol. 33, *European Southern Observatory Conference and Workshop Proceedings*, ed. B. Reipurth, 233–246
- Hillenbrand, L. A. & Findeisen, K. P. 2015, *ApJ*, 808, 68
- Ida, S., Guillot, T., & Morbidelli, A. 2016, *A&A*, 591, A72
- Jørgensen, J. K., Bourke, T. L., Myers, P. C., Di Francesco, J., van Dishoeck, E. F., Lee, C.-F., Ohashi, N., Schöier, F. L., Takakuwa, S., Wilner, D. J., & Zhang, Q. 2007, *ApJ*, 659, 479
- Jørgensen, J. K., van Dishoeck, E. F., Visser, R., Bourke, T. L., Wilner, D. J., Lommen, D., Hogerheijde, M. R., & Myers, P. C. 2009, *A&A*, 507, 861
- Kamp, I., Dullemond, C. P., Hogerheijde, M., & Enriquez, J. E. 2005, in *IAU Symposium*, Vol. 231, *Astrochemistry: Recent Successes and Current Challenges*, ed. D. C. Lis, G. A. Blake, & E. Herbst, 377–386
- Kanagawa, K. D., Muto, T., Tanaka, H., Tanigawa, T., Takeuchi, T., Tsukagoshi, T., & Momose, M. 2015, *ApJ*, 806, L15
- , 2016, *PASJ*, 68, 43
- Kataoka, A., Okuzumi, S., Tanaka, H., & Nomura, H. 2014, *A&A*, 568, A42
- Kataoka, A., Tanaka, H., Okuzumi, S., & Wada, K. 2013, *A&A*, 557, L4
- Kimura, S. S., Kunitomo, M., & Takahashi, S. Z. 2016, *MNRAS*, 461, 2257
- Kimura, S. S. & Tsuribe, T. 2012, *PASJ*, 64, 116
- Kitamura, Y., Momose, M., Yokogawa, S., Kawabe, R., Tamura, M., & Ida, S. 2002, *ApJ*, 581, 357
- Kornet, K., Stepinski, T. F., & Różyczka, M. 2001, *A&A*, 378, 180
- Krijt, S., Ormel, C. W., Dominik, C., & Tielens, A. G. G. M. 2016, *A&A*, 586, A20
- Kunz, M. W. & Lesur, G. 2013, *MNRAS*, 434, 2295
- Kusaka, T., Nakano, T., & Hayashi, C. 1970, *Progress of Theoretical Physics*, 44, 1580
- Kwon, W., Looney, L. W., Mundy, L. G., Chiang, H.-F., & Kemball, A. J. 2009, *ApJ*, 696, 841
- Lambrechts, M. & Johansen, A. 2012, *A&A*, 544, A32
- , 2014, *A&A*, 572, A107
- Laughlin, G. & Bodenheimer, P. 1994, *ApJ*, 436, 335
- Levison, H. F. & Morbidelli, A. 2003, *Nature*, 426, 419
- Lomax, O., Whitworth, A. P., Hubber, D. A., Stamatellos, D., & Walch, S. 2014, *MNRAS*, 439, 3039
- Lommen, D., Jørgensen, J. K., van Dishoeck, E. F., & Crapsi, A. 2008, *A&A*, 481, 141
- Machida, M. N., Inutsuka, S., & Matsumoto, T. 2008, *ApJ*, 676, 1088
- , 2010, *ApJ*, 724, 1006
- , 2011, *PASJ*, 63, 555
- Malhotra, R. 1995, *AJ*, 110, 420
- Masson, J., Chabrier, G., Hennebelle, P., Vaytet, N., & Commerçon, B. 2016, *A&A*, 587, A32
- Mathis, J. S., Rumpl, W., & Nordsieck, K. H. 1977, *ApJ*, 217, 425
- Matsumoto, T. & Hanawa, T. 2003, *ApJ*, 595, 913
- McClure, M. K., Bergin, E. A., Cleeves, L. I., van Dishoeck, E. F., Blake, G. A., Evans, II, N. J., Green, J. D., Henning, T., Öberg, K. I., Pontoppidan, K. M., & Salyk, C. 2016, *ApJ*, 831, 167
- Mercer, A. & Stamatellos, D. 2017, *MNRAS*, 465, 2
- Miotello, A., Testi, L., Lodato, G., Ricci, L., Rosotti, G., Brooks, K., Maury, A., & Natta, A. 2014, *A&A*, 567, A32
- Miotello, A., van Dishoeck, E. F., Williams, J. P., Ansdell, M., Guidi, G., Hogerheijde, M., Manara, C. F., Tazzari, M., Testi, L., van der Marel, N., & van Terwisga, S. 2016, *ArXiv e-prints*
- Miyake, K. & Nakagawa, Y. 1993, *Icarus*, 106, 20
- Murillo, N. M., Lai, S.-P., Bruderer, S., Harsono, D., & van Dishoeck, E. F. 2013, *A&A*, 560, A103
- Nakagawa, Y., Sekiya, M., & Hayashi, C. 1986, *Icarus*, 67, 375
- Nakamoto, T. & Nakagawa, Y. 1994, *ApJ*, 421, 640
- Nayakshin, S. 2010, *MNRAS*, 408, L36
- Ohashi, N., Saigo, K., Aso, Y., Aikawa, Y., Koyamatsu, S., Machida, M. N., Saito, M., Takahashi, S. Z., Takakuwa, S., Tomida, K., Tomisaka, K., & Yen, H.-W. 2014, *ApJ*, 796, 131
- Okuzumi, S., Momose, M., Sirono, S.-i., Kobayashi, H., & Tanaka, H. 2016, *ApJ*, 821, 82
- Okuzumi, S., Tanaka, H., Kobayashi, H., & Wada, K. 2012, *ApJ*, 752, 106
- Ormel, C. W. & Klahr, H. H. 2010, *A&A*, 520, A43
- Ormel, C. W., Spaans, M., & Tielens, A. G. G. M. 2007, *A&A*, 461, 215
- Pätzold, M., Andert, T., Hahn, M., Asmar, S. W., Barriot, J.-P., Bird, M. K., Häusler, B., Peter, K., Tellmann, S., Grün, E., Weissman, P. R., Sierks, H., Jorda, L., Gaskell, R., Preusker, F., & Scholten, F. 2016, *Nature*, 530, 63
- Pérez, L. M., Carpenter, J. M., Andrews, S. M., Ricci, L., Isella, A., Linz, H., Sargent, A. I., Wilner, D. J., Henning, T., Deller, A. T., Chandler, C. J., Dullemond, C. P., Lazio, J., Menten, K. M., Corder, S. A., Storm, S., Testi, L., Tazzari, M., Kwon, W., Calvet, N., Greaves, J. S., Harris, R. J., & Mundy, L. G. 2016, *Science*, 353, 1519
- Pérez, L. M., Carpenter, J. M., Chandler, C. J., Isella, A., Andrews, S. M., Ricci, L., Calvet, N., Corder, S. A., Deller, A. T., Dullemond, C. P., Greaves, J. S., Harris, R. J., Henning, T., Kwon, W., Lazio, J., Linz, H., Mundy, L. G., Sargent, A. I., Storm, S., Testi, L., & Wilner, D. J. 2012, *ApJ*, 760, L17
- Pérez, L. M., Chandler, C. J., Isella, A., Carpenter, J. M., Andrews, S. M., Calvet, N., Corder, S. A., Deller, A. T., Dullemond, C. P., Greaves, J. S., Harris, R. J., Henning, T., Kwon, W., Lazio, J., Linz, H., Mundy, L. G., Ricci, L., Sargent, A. I., Storm, S., Tazzari, M., Testi, L., & Wilner, D. J. 2015, *ApJ*, 813, 41

- Pollack, J. B., Hollenbach, D., Beckwith, S., Simonelli, D. P., Roush, T., & Fong, W. 1994, *ApJ*, 421, 615
- Price, D. J., Tricco, T. S., & Bate, M. R. 2012, *MNRAS*, 423, L45
- Ricci, L., Testi, L., Natta, A., & Brooks, K. J. 2010a, *A&A*, 521, A66
- Ricci, L., Testi, L., Natta, A., Neri, R., Cabrit, S., & Herczeg, G. J. 2010b, *A&A*, 512, A15
- Sakai, N., Sakai, T., Hirota, T., Watanabe, Y., Ceccarelli, C., Kahane, C., Bottinelli, S., Caux, E., Demyk, K., Vastel, C., Coutens, A., Taquet, V., Ohashi, N., Takakuwa, S., Yen, H.-W., Aikawa, Y., & Yamamoto, S. 2014, *Nature*, 507, 78
- Sandell, G. & Weintraub, D. A. 2001, *ApJS*, 134, 115
- Sato, T., Okuzumi, S., & Ida, S. 2016, *A&A*, 589, A15
- Shakura, N. I. & Sunyaev, R. A. 1973, *A&A*, 24, 337
- Stamatellos, D. & Whitworth, A. P. 2008, *A&A*, 480, 879
- . 2009, *MNRAS*, 392, 413
- Stamatellos, D., Whitworth, A. P., & Hubber, D. A. 2012, *MNRAS*, 427, 1182
- Takahashi, S. Z. & Inutsuka, S. 2014, *ApJ*, 794, 55
- . 2016, *AJ*, 152, 184
- Takahashi, S. Z., Inutsuka, S., & Machida, M. N. 2013, *ApJ*, 770, 71
- Takahashi, S. Z., Tsukamoto, Y., & Inutsuka, S. 2016, *MNRAS*, 458, 3597
- Takakuwa, S., Saito, M., Lim, J., Saigo, K., Sridharan, T. K., & Patel, N. A. 2012, *ApJ*, 754, 52
- Takeuchi, T., Clarke, C. J., & Lin, D. N. C. 2005, *ApJ*, 627, 286
- Tazzari, M., Testi, L., Ercolano, B., Natta, A., Isella, A., Chandler, C. J., Pérez, L. M., Andrews, S., Wilner, D. J., Ricci, L., Henning, T., Linz, H., Kwon, W., Corder, S. A., Dullemond, C. P., Carpenter, J. M., Sargent, A. I., Mundy, L., Storm, S., Calvet, N., Greaves, J. A., Lazio, J., & Deller, A. T. 2016, *A&A*, 588, A53
- Tobin, J. J., Hartmann, L., Chiang, H.-F., Wilner, D. J., Looney, L. W., Loinard, L., Calvet, N., & D'Alessio, P. 2012, *Nature*, 492, 83
- . 2013, *ApJ*, 771, 48
- Tobin, J. J., Kratter, K. M., Persson, M. V., Looney, L. W., Dunham, M. M., Segura-Cox, D., Li, Z.-Y., Chandler, C. J., Sadavoy, S. I., Harris, R. J., Melis, C., & Pérez, L. M. 2016, *Nature*, 538, 483
- Tomida, K., Machida, M. N., Hosokawa, T., Sakurai, Y., & Lin, C. H. 2017, *ApJ*, 835, L11
- Tomida, K., Okuzumi, S., & Machida, M. N. 2015, *ApJ*, 801, 117
- Toomre, A. 1964, *ApJ*, 139, 1217
- Tsukamoto, Y. 2011, *Icarus*, 212, 911
- . 2016, *PASA*, 33, e010
- Tsukamoto, Y., Iwasaki, K., Okuzumi, S., Machida, M. N., & Inutsuka, S. 2015a, *ApJ*, 810, L26
- . 2015b, *MNRAS*, 452, 278
- Tsukamoto, Y. & Machida, M. N. 2011, *MNRAS*, 416, 591
- . 2013, *MNRAS*, 428, 1321
- Tsukamoto, Y., Machida, M. N., & Inutsuka, S. 2013, *MNRAS*, 436, 1667
- Tsukamoto, Y., Takahashi, S. Z., Machida, M. N., & Inutsuka, S. 2015c, *MNRAS*, 446, 1175
- Vorobyov, E. I. 2009, *ApJ*, 704, 715
- Vorobyov, E. I. & Basu, S. 2006, *ApJ*, 650, 956
- . 2010a, *ApJ*, 714, L133
- . 2010b, *ApJ*, 719, 1896
- Wada, K., Tanaka, H., Okuzumi, S., Kobayashi, H., Suyama, T., Kimura, H., & Yamamoto, T. 2013, *A&A*, 559, A62
- Warren, S. G. 1984, *Appl. Opt.*, 23, 1206
- Weidenschilling, S. J. 1977, *MNRAS*, 180, 57
- Weingartner, J. C. & Draine, B. T. 2001, *ApJ*, 548, 296
- Williams, J. P. & Cieza, L. A. 2011, *ARA&A*, 49, 67
- Wurster, J., Price, D. J., & Bate, M. R. 2016, *MNRAS*, 457, 1037
- Yen, H.-W., Koch, P. M., Takakuwa, S., Krasnopolsky, R., Ohashi, N., & Aso, Y. 2017, *ApJ*, 834, 178
- Yen, H.-W., Liu, H. B., Gu, P.-G., Hirano, N., Lee, C.-F., Puspitaningrum, E., & Takakuwa, S. 2016, *ApJ*, 820, L25
- Yen, H.-W., Takakuwa, S., Ohashi, N., Aikawa, Y., Aso, Y., Koyamatsu, S., Machida, M. N., Saigo, K., Saito, M., Tomida, K., & Tomisaka, K. 2014, *ApJ*, 793, 1
- Youdin, A. N. & Lithwick, Y. 2007, *Icarus*, 192, 588
- Zhang, K., Bergin, E. A., Blake, G. A., Cleeves, L. I., Hogerheijde, M., Salinas, V., & Schwarz, K. R. 2016, *ApJ*, 818, L16
- Zhang, K., Blake, G. A., & Bergin, E. A. 2015, *ApJ*, 806, L7
- Zubko, V. G., Mennella, V., Colangeli, L., & Bussolletti, E. 1996, *MNRAS*, 282, 1321